

A new fitting function for GRB MeV spectra based on the internal shock synchrotron model

M. Yassine^{1,2}, F. Piron³, F. Daigne⁴, R. Mochkovitch⁴, F. Longo^{1,2}, N. Omodei⁵, and G. Vianello⁵

¹ Istituto Nazionale di Fisica Nucleare, Sezione di Trieste, I-34127 Trieste, Italy

² Dipartimento di Fisica, Università di Trieste, I-34127 Trieste, Italy
e-mail: mychbib@gmail.com, francesco.longo@ts.infn.it

³ Laboratoire Univers et Particules de Montpellier, Université de Montpellier, CNRS/IN2P3, Montpellier, France
e-mail: piron@in2p3.fr

⁴ UPMC-CNRS, UMR7095, Institut d'Astrophysique de Paris, 75014 Paris, France
e-mail: daigne@iap.fr, mochko@iap.fr

⁵ W. W. Hansen Experimental Physics Laboratory, Kavli Institute for Particle Astrophysics and Cosmology, Department of Physics and SLAC National Accelerator Laboratory, Stanford University, Stanford, CA 94305, USA

ABSTRACT

Aims. The physical origin of the GRB prompt emission is still a subject of debate. Internal shock models have been widely explored owing to their ability to explain most of the high-energy properties of this emission phase. While the Band function or other phenomenological functions are commonly used to fit GRB prompt emission spectra, we propose a new parametric function that is inspired by an internal shock physical model. We use this function as a proxy of the model to confront it easily to GRB observations.

Methods. We built a parametric function that represents the spectral form of the synthetic bursts provided by our internal shock synchrotron model (ISSM). We simulated the response of the *Fermi* instruments to the synthetic bursts and fitted the obtained count spectra to validate the ISSM function. Then, we applied this function to a sample of 74 bright GRBs detected by the *Fermi*/GBM, and we computed the width of their spectral energy distributions around their peak energy. For comparison, we fitted also the phenomenological functions that are commonly used in the literature. Finally, we performed a time-resolved analysis of the broadband spectrum of GRB 090926A, which was jointly detected by the *Fermi* GBM and LAT. This spectrum has a complex shape and exhibits a power-law component with an exponential cutoff at high energy, which is compatible with inverse Compton emission attenuated by gamma-ray internal absorption.

Results. This work proposes a new parametric function for spectral fitting that is based on a physical model. The ISSM function reproduces 81% of the spectra in the GBM bright GRB sample, versus 59% for the Band function, for the same number of parameters. It gives also relatively good fits to the GRB 090926A spectra. The width of the MeV spectral component that is obtained from the fits of the ISSM function is slightly larger than the width from the Band fits, but it is smaller when observed over a wider energy range. Moreover, all of the 74 analysed spectra are found to be significantly wider than the synthetic synchrotron spectra. We discuss possible solutions to reconcile the observations with the internal shock synchrotron model, such as an improved modeling of the shock micro-physics or more accurate spectral measurements at MeV energies.

Key words. gamma-ray bursts – internal shock model – prompt emission – synchrotron and inverse Compton radiations

1. Introduction

Gamma-ray bursts (GRBs) were discovered more than fifty years ago, and they are the most electro-magnetic events ever observed in the Universe. They are brief flashes of high-energy radiation emitted by an ultra-relativistic collimated outflow which is thought to originate from a stellar-mass black hole formed by the merging of binary systems (Nakar 2007; D'Avanzo 2015) or the explosions of massive stars (Woosley & Bloom 2006; Stanek et al. 2003; Kawabata et al. 2003; Hjorth et al. 2003; Bloom et al. 2002; Hjorth et al. 2005; Gehrels et al. 2005; Abbott et al. 2017). GRB emission is observed in two successive phases, a short phase of intense radiation followed by a long-lived afterglow phase. While both emissions are essentially non thermal, the prompt phase is notably characterized by the irregular shape and the fast variability of its temporal profile. Despite substantial efforts in modeling the GRB prompt emission, different scenarios such as internal shocks (Rees & Meszaros 1994), dissipative photospheres (Beloborodov & Mészáros 2017) or reconnection above the photosphere (Giannios 2008; McKinney & Uzdensky 2012; Sironi et al. 2015; Beniamini & Granot 2016) have been proposed to explain its physical origin. Internal shock models have been explored in detail (Kobayashi et al. 1997; Daigne & Mochkovitch 1998; Bošnjak et al. 2009; Daigne et al. 2011; Bošnjak & Daigne 2014) owing to their ability to produce emissions from the visible to the GeV domain and to account for GRB observed properties such as their spectral evolution and the extreme variability seen in their light curves. In this class of models, the GRB relativistic outflow converts a fraction of its kinetic energy into internal energy through internal shocks, which occur when the distribution of the Lorentz factors in the flow

is highly non-uniform. Part of the energy that is dissipated in the shocks is transferred to a fraction of the electrons which emit non-thermal synchrotron and inverse Compton radiations.

Since the launch of the *Fermi* satellite in June 2008, the GRB high-energy emission has been studied with great sensitivity. The Large Area Telescope (LAT, 20 MeV- 300 GeV, (Atwood et al. 2009)) has detected more than 180 GRBs (Ajello et al. 2019) thanks to its wide field of view (2.4 sr), its large effective area ($\sim 0.9 \text{ m}^2$ above $\sim 1 \text{ GeV}$) and to the improved event reconstruction (Pass 8 hereafter) that has been implemented in 2015 (Atwood et al. 2013). The Gamma-ray Burst Monitor (GBM) is the second instrument onboard *Fermi* and it consists of 12 sodium iodide (NaI, 8 keV - 1 MeV) and 2 bismuth germanate (BGO, 250 keV-40 MeV) detectors placed around the *Fermi* spacecraft. The GBM monitors continuously a large portion of the sky (9.5 sr), and it has detected more than 2600 GRBs so far (Narayana Bhat et al. 2016). Together, the GBM and the LAT cover more than seven decades in energy, hence they are the most suitable instruments currently in operations to study the broadband high-energy emission of GRBs.

The keV-MeV spectral component of GRBs, which is often attributed to synchrotron emission, is commonly fitted by the phenomenological Band function (Band et al. 1993). Despite its ability to describe many of the GRB non-thermal spectra, this function has little physical grounds and is not suitable for a fair fraction of spectra (see, e.g., Gruber et al. (2014)). The interpretation of the GRB spectral fit results faces another problem that has been pointed out twenty years ago by Preece et al. (1998) (see also Crider et al. (1997); Ghisellini et al. (2000); Burgess et al. (2015)). In their analysis of CGRO/BATSE bursts, these authors came to the conclusion that most of the fitted spectral slopes are too hard to be compatible with the expectations from the synchrotron theory at low energy, an issue that is now referred to as the “synchrotron line-of-death problem” (Ghisellini et al. 2000; Axelsson & Borgonovo 2015; Burgess et al. 2015).

More recently, Yu et al. (2015) and Axelsson & Borgonovo (2015) used the spectral sharpness to show that the spectrum that is expected from an electron synchrotron model is wider than the Band spectra of most GRBs detected by the GBM, calling for a new physical interpretation of the keV-MeV spectral component. However, it should be noted that the theoretical spectrum considered in Yu et al. (2015) was essentially derived from a pure Maxwellian electron distribution, which does not account for the dynamical evolution of the electron and photon distributions in the GRB jet. In addition, the authors did not attempt to fit this theoretical model to the data, which might introduce instrumental biases in the comparison with the Band fit results. Actually, direct fits of the synchrotron emission model to GRB prompt spectra have been performed by Zhang et al. (2016) and Burgess (2019), who showed that the line-of-death and spectral sharpness issues are likely artefacts due to the use of the Band function. In the same spirit, this work compares the predictions of an actual internal shock synchrotron model to the observations.

In this work, we investigated the version of the internal shock model described in Daigne & Mochkovitch (1998); Bošnjak et al. (2009); Daigne et al. (2011); Bošnjak & Daigne (2014). We simulated synthetic bursts provided by this model using the GBM and LAT detector responses. The characteristics of the synthetic bursts and our simulation procedure are described in Sect. 2. In Sect. 3 we present the functions used to fit the burst spectra, including a new fitting function (called ISSM hereafter) that is directly built from the synthetic spectra in the keV-MeV energy range. The spectral analysis of the synthetic bursts and the computation of their spectral width are reported in Sect. 4. In Sect. 5, we apply the same set of fitting functions to a sample of 74 GBM bright GRBs. The data selection and the technique of identification of the best fit spectral model are presented, as well as a focus on the spectral parameters and sharpness obtained for the Band and ISSM functions. In Sect. 6 we revisit the spectral analysis of GRB 090926A using the new ISSM function. This burst was bright in the GBM and LAT instruments, and it exhibits fast variability above 100 MeV during the keV-MeV prompt emission. As reported in (Yassine et al. 2017) (Y17 hereafter), it constitutes an ideal case to test the internal shock model from keV to GeV energies. Finally, we discuss our results in Sect. 7 and give our conclusions in Sect. 8.

2. Simulation of the synthetic bursts

2.1. The internal shock model

The version of the internal shock model that we used is able to reproduce most of the GRB properties, in particular the variability timescales and the shape of the GRB light curves (Daigne & Mochkovitch 1998). In this model, the GRB outflow consists of a set of solid layers which move at different Lorentz factors, whose collisions mimick the propagation of an internal shock wave along the GRB jet. Each GRB is characterized by its redshift, duration and kinetic energy, and by a Lorentz factor profile. The model also assumes that some fraction ϵ_B of the energy dissipated in the shocks is transferred to the magnetic field, and that a fair fraction ϵ_e is injected into a small part ζ of accelerated electrons. The energy distribution of the accelerated electrons is a power law with a slope $-p$ which is set to a value ranging from -2.9 to -2.3 . This adopted interval for the index of the electron distribution corresponds to a typical high energy spectral index $\beta=-(p/2+1)$ between 2.15 and 2.45 as observed (Daigne & Mochkovitch 1998). In addition to the GRB outflow dynamics, the model accounts for the main radiative processes at high energy. The numerical code that simulates the shock dynamics has been coupled to a radiative code, which follows the evolution of the electron and photon distributions in order to produce realistic light curves and spectra from keV to GeV energies in the observer frame (Bošnjak et al. 2009). The radiative processes include the synchrotron emission from the accelerated electrons and the inverse Compton (IC) scatterings in the Thomson and Klein-Nishina regimes. Synchrotron self-absorption at low energy and photon-photon annihilation at high energy are also accounted for.

2.2. Characteristics of the bursts

The synthetic burst that we considered corresponds to the case B of (Bošnjak & Daigne 2014) (BD14 hereafter) owing to its typical kinetic energy, $E_k=10^{54}$ erg, and to its brightness in the LAT energy range. The burst is long, with a duration of 15 s, and it is bright during the first 6 s only. The microphysical parameters describing the electron distribution are $\epsilon_e = 1/3$, $p = 2.7$, and a varying fraction ζ of accelerated particles. The low magnetic energy density ($\epsilon_B=10^{-3}$) enhances the IC component and makes this burst an interesting candidate for a LAT detection. The burst has an isotropic equivalent energy $E_{\gamma,iso} = 1.35 \times 10^{52}$ erg, with 1.26×10^{52} erg in the synchrotron component and 0.09×10^{52} erg in the IC component. The low and high-energy indices of the synchrotron spectrum are ~ -1.1 and ~ -2.4 , respectively.

We placed the synthetic burst at a low redshift $z = 0.07$ as an easy way to increase the observed flux and to produce a large number of simulated counts in the *Fermi* instruments. As explained further below, this allowed us to characterize with high accuracy and unambiguously the properties of the burst emission folded with the instrument responses. As a result, the fluence of the synthetic burst is 5.4×10^{-4} erg cm $^{-2}$ between 10 keV and 1 MeV during the first 6 s. This would be a very rare event among the GRBs that have been jointly detected by the GBM and the LAT, whose fluence ranges from 5×10^{-8} erg cm $^{-2}$ to $\sim 3 \times 10^{-4}$ erg cm $^{-2}$ in the same energy range (Ackermann et al. 2013). In order to consider more realistic situations, two other synthetic bursts were created by dividing the simulated emission flux by 10 and 100.

In the following, the three synthetic bursts are denoted by GRB_B001, GRB_B010 and GRB_B100 in order of decreasing flux. We splitted the light curve of each of these bursts in three time intervals, [0 s, 1 s], [1 s, 3 s] and [3 s, 6 s]. The upper panel in the left part of Fig. 1 shows the corresponding spectral energy distributions (SEDs) of GRB_B010 in addition to the SED of this burst during the total time interval [0 s, 6 s]. The lower panel shows the evolution with energy of the local photon index $\Gamma(E)$, which we calculated numerically as the logarithmic derivative of the differential photon spectrum $F = dN/dE$ with respect to the logarithmic energy, $\Gamma(E) = \partial \ln(F)/\partial \ln(E)$.

2.3. Simulation procedure

We simulated the signal of the synthetic bursts as it would be observed by the GBM or the LAT by performing a convolution of the GRB differential photon spectra dN/dE with the corresponding detector response matrix (DRM). The DRM is defined as the detector effective area $A_{\text{eff}}(E)$ multiplied by its energy redistribution function $D(E, E')$, where E and E' stand for true and measured photon energy, respectively. The mean number of counts in the interval of measured energy $[E'_{\text{min}}, E'_{\text{max}}]$ is given by:

$$N = T_{\text{obs}} \int_{E'_{\text{min}}}^{E'_{\text{max}}} dE' \int_0^{+\infty} \frac{dN}{dE}(E) A_{\text{eff}}(E) D(E, E') dE \quad (1)$$

where T_{obs} is the time exposure. For this computation, we used the DRMs of the four GBM detectors (NaI6, 7, 8 and BGO1) that have seen GRB 090926A and the DRM of the LAT produced by the *gtrspgen*¹ tool available at the *Fermi* Science Support Center². The simulation of the synthetic bursts was performed with the *XSPEC* software³ (version 12.8.2), which generates Poisson counts of detected photons. For simplicity, we did not add any background to the burst signal since it has a negligible effect owing to the large fluence of the simulated bursts. The multi-detector light curve of the synthetic burst GRB_B010 is shown in the right part of Fig. 1.

3. Spectral models

The GRB spectra that we analyzed were fitted with several phenomenological functions that are commonly found in the literature, and with a new parametric function that is built from the synthetic spectra. All of the functions presented below are normalized by an amplitude parameter A , in units of cm $^{-2}$ s $^{-1}$ keV $^{-1}$.

3.1. Phenomenological models

3.1.1. Band function

The Band function (Band et al. 1993) is often used to fit the keV-MeV spectrum of GRBs. It is composed of two smoothly-connected power laws with four parameters A_{Band} , α , β and E_p , and it is defined as:

$$\frac{dN_{\text{Band}}}{dE}(E) = A_{\text{Band}} \begin{cases} \left(\frac{E}{100 \text{ keV}}\right)^\alpha \exp\left[-\frac{E(2+\alpha)}{E_p}\right], & E \leq E_b = E_p \frac{\alpha-\beta}{2+\alpha} \\ \left(\frac{E}{100 \text{ keV}}\right)^\beta \left[\frac{E_p}{100 \text{ keV}} \frac{\alpha-\beta}{2+\alpha}\right]^{\alpha-\beta} \exp[\beta - \alpha], & E > E_b = E_p \frac{\alpha-\beta}{2+\alpha}. \end{cases} \quad (2)$$

¹ <https://fermi.gsfc.nasa.gov/ssc/data/analysis/scitools/help/gtrspgen.txt>

² <https://fermi.gsfc.nasa.gov/ssc/data/analysis/scitools/overview.html>

³ <https://heasarc.nasa.gov/docs/xanadu/xspec>

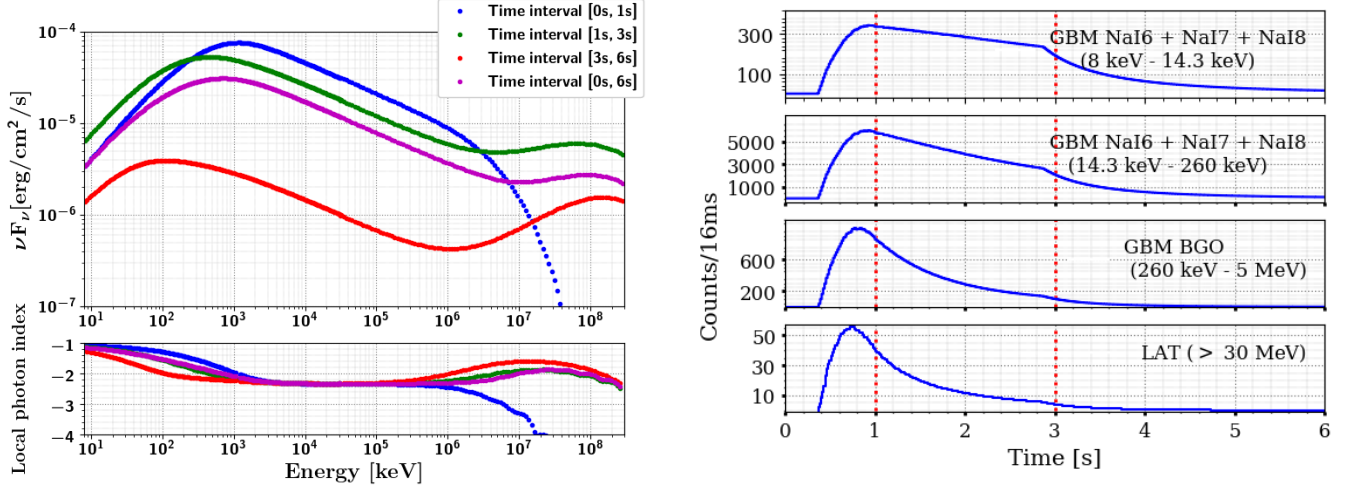


Fig. 1. Left: Spectral energy distributions of the synthetic burst GRB_B010 and local photon index in the four time intervals [0 s, 1 s], [1 s, 3 s], [3 s, 6 s] and [0 s, 6 s]. Right: Multi-detector light curves of GRB_B010: summed counts in two energy ranges of GBM/NaI detectors (first two panels), in the GBM/BGO energy range (third panel) and using the largest LAT energy range (> 30 MeV) (bottom panel). The red dashed lines show the boundaries of the three time intervals [0 s, 1 s], [1 s, 3 s] and [3 s, 6 s].

The local photon index of this function reads:

$$\Gamma_{\text{Band}}(E) = \begin{cases} \alpha - \frac{(2+\alpha)}{E_p} E, & E \leq E_b \\ \beta, & E > E_b. \end{cases} \quad (3)$$

3.1.2. Logarithmic parabola and variants

The log-parabola function (LP hereafter) has three free parameters, i.e. one less than the Band function. It was suggested by (Massaro et al. 2010) to fit GRB spectra and it is expressed as:

$$\frac{dN_{\text{LP}}}{dE}(E) = A_{\text{LP}} \left(\frac{E}{E_0} \right)^{-\gamma - \beta \log(E/E_0)} \quad (4)$$

where E_0 is a fixed reference energy. The local photon index is a function of the spectral parameters γ and β :

$$\Gamma_{\text{LP}}(E) = -\gamma - 2\beta \log \left(\frac{E}{E_0} \right) \quad (5)$$

and the LP peak energy is $E_p = E_0 \times 10^{\frac{2-\gamma}{2\beta}}$. The LP function is characterized by its continuous curvature, unlike the Band function. Its symmetric shape implies that the spectral parameter reconstruction is driven by the low-energy data, where most of the photon statistics is recorded. In order to gain some latitude at high energies, we modified the function to freeze the local photon index above a break energy E_b . As a result, the modified logarithmic parabola, denoted by LP1 hereafter, has four free parameters:

$$\frac{dN_{\text{LP1}}}{dE}(E) = A_{\text{LP1}} \begin{cases} \left(\frac{E}{E_0} \right)^{-\gamma - \beta \log(E/E_0)}, & E \leq E_b \\ \left(\frac{E_b}{E_0} \right)^{-\gamma - \beta \log(E_b/E_0)} \times \left(\frac{E}{E_b} \right)^{-\gamma - 2\beta \log(E_b/E_0)}, & E > E_b \end{cases} \quad (6)$$

We introduced a similar modification at low energies, which relaxes the dependency of the spectral fit around the peak energy on the low-energy data. The corresponding modified logarithmic parabola, denoted by LP2 hereafter, has five free parameters:

$$\frac{dN_{\text{LP2}}}{dE}(E) = A_{\text{LP2}} \begin{cases} \left(\frac{E'_b}{E_0} \right)^{-\gamma - \beta \log(E'_b/E_0)} \times \left(\frac{E}{E'_b} \right)^{-\gamma - 2\beta \log(E'_b/E_0)}, & E \leq E'_b \\ \left(\frac{E}{E_0} \right)^{-\gamma - \beta \log(E/E_0)}, & E'_b \leq E \leq E_b \\ \left(\frac{E_b}{E_0} \right)^{-\gamma - \beta \log(E_b/E_0)} \times \left(\frac{E}{E_b} \right)^{-\gamma - 2\beta \log(E_b/E_0)}, & E > E_b \end{cases} \quad (7)$$

3.1.3. (Broken) power law with exponential cutoff

For the spectral analysis of GRB 090926A presented in Sect. 6, which extends to the LAT energy range, we adopted either a power law with exponential cutoff (CUTPL) or a broken power law with exponential cutoff (CUTBPL). The CUTPL function is expressed as:

$$\frac{dN_{\text{CUTPL}}}{dE}(E) = A_{\text{CUTPL}} \left(\frac{E}{E_0} \right)^\lambda \exp \left(-\frac{E}{E_f} \right) \quad (8)$$

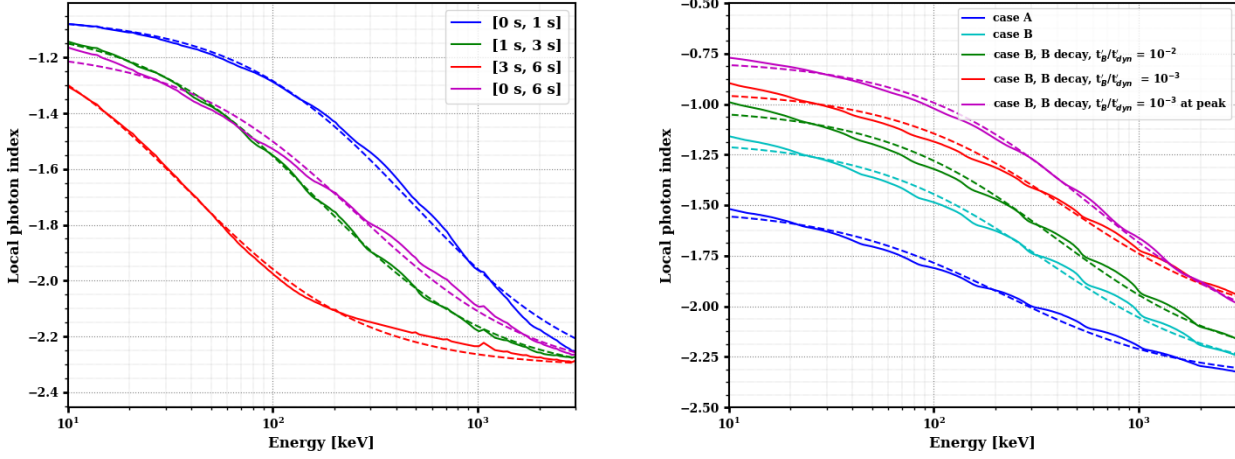


Fig. 2. Left: Least-square fit (dashed lines) of Eq. 10 to the local photon index (thick lines) in the keV-MeV range for the four time intervals of the synthetic burst GRB_B001. Right: Least-square fit (dashed line) to the local photon index (solid line) in the keV-MeV range for several synthetic bursts: time integrated spectrum of two reference cases presented in BD14, case A (blue) and B (cyan) with a varying fraction of accelerated electrons and $p = 2.7$. Case A corresponds to the most standard fast cooling synchrotron spectrum, and case B to a modified synchrotron spectrum affected by inverse Compton scattering in the Klein-Nishina regime. In addition, preliminary calculation of the same case B taking into account a magnetic field decay in the emission region are also presented (taken from Daigne & Bošnjak, in preparation) with a time scale of the decay $t'_B/t'_{\text{dyn}} = 10^{-2}$ (green) or 10^{-3} (red), where t'_{dyn} is the dynamical timescale. Finally, the same case is also shown for a time interval of 0.25 s around the peak of the light curve (magenta).

which has three free parameters A_{CUTBPL} , λ and the folding energy E_f of the exponential cutoff, and a fixed reference energy E_0 . The CUTBPL function is expressed as:

$$\frac{dN_{\text{CUTBPL}}}{dE}(E) = A_{\text{CUTBPL}} \begin{cases} \left(\frac{E}{E_0}\right)^{\gamma_0} \exp\left(-\frac{E}{E_f}\right), & E \leq E_b \\ \left(\frac{E_b}{E_0}\right)^{\gamma_0} \left(\frac{E}{E_b}\right)^{\gamma} \exp\left(-\frac{E}{E_f}\right), & E > E_b \end{cases} \quad (9)$$

where E_b is the break energy, γ_0 and γ are the photon index below and above E_b , respectively. As explained in Y17, the break energy and the photon spectral index below the break have been fixed to $E_b = 200$ keV and $\gamma_0 = +4$ in order to cancel the contribution of the power-law component at low energies, as for instance expected from an inverse Compton spectral component that would extend the synchrotron spectrum at high energies only. As a result, the CUTBPL function has the same number of free parameters as the CUTPL function.

3.2. The ISSM spectral model

In order to build a function that is representative of the synchrotron spectral component of the synthetic bursts, we fitted their local photon index as a function of energy with the following parameterization:

$$\Gamma(E) = \frac{\partial \ln(F)}{\partial \ln(E)} = -a + \frac{b}{E + c} \quad (10)$$

where a , b , c are free parameters. This parameterization adequately fits the local photon index of GRB_B001 in the four time intervals as shown in the left panel of Fig. 2. The right panel of this figure shows that it is also suitable for different configurations of the model presented in BD14. Note that the synthetic bursts using various assumptions for the microphysics in the emission region do not have the same low-energy photon index: ~ -1.5 for case A as expected for the standard fast cooling synchrotron spectrum, and -1.1 to -0.75 for case B. Integrating Eq. 10, one gets:

$$F(E) = F(E_r) \exp\left[-a \ln\left(\frac{E}{E_r}\right)\right] \exp\left[\frac{b}{c} \ln\left(\frac{E(E_r + c)}{E_r(E + c)}\right)\right] \quad (11)$$

where the reference energy E_r is related to the constant of integration. From this parameterization, the asymptotic spectral indices towards low and high energies can be easily obtained as $\alpha = \frac{b}{c} - a$ and $\beta = -a$, respectively. Finally, defining the SED peak energy E_p as the solution of $\Gamma(E) = -2$:

$$E_p = -c \left(\frac{2 + \alpha}{2 + \beta} \right), \quad (12)$$

one can rewrite Eq. 11 to obtain a new expression, denoted by ISSM hereafter:

$$\frac{dN_{\text{ISSM}}}{dE}(E) = \frac{A_{\text{ISSM}}}{\left[1 - \frac{E_p}{E_r} \left(\frac{2+\beta}{2+\alpha}\right)\right]^{\beta-\alpha}} \times \left(\frac{E}{E_r}\right)^\alpha \left[\frac{E}{E_r} - \frac{E_p}{E_r} \left(\frac{2+\beta}{2+\alpha}\right)\right]^{\beta-\alpha} \quad (13)$$

which has four parameters A_{ISSM} , α , β , E_p . It is important to note that E_r is a fixed reference energy which is chosen as the energy at which the flux normalization is defined:

$$\frac{dN_{\text{ISSM}}}{dE}(E_r) = A_{\text{ISSM}}. \quad (14)$$

In other words, different choices of E_r only affect the flux normalization parameter A_{ISSM} and not the shape of the ISSM function. The local photon index is given by:

$$\Gamma_{\text{ISSM}}(E) = \alpha + (\beta - \alpha) \frac{E}{E - E_p \left(\frac{2+\beta}{2+\alpha}\right)}. \quad (15)$$

The four parameters of the ISSM (flux normalization, SED peak energy and asymptotic slopes) resemble those of the Band function. The local photon index $\Gamma_{\text{ISSM}}(E)$ decreases continuously with energy and the ISSM function is continuously curved unlike the Band function, and unlike simplified versions of the synchrotron model based on pure power-law energy distributions of the accelerated electrons. In the framework of our internal shock synchrotron model, the spectral curvature arises essentially from the superposition of instantaneous electron synchrotron spectra which vary significantly within the time intervals considered by the observer, owing to the dynamical evolution in the shock region. While we only tested the ISSM function on a simple, single-pulse burst, we are confident that it can also represent complex burst spectra resulting from various distributions of the Lorentz factor. Indeed, in most cases, complex bursts can be interpreted in terms of a succession of individual pulses so that time-dependent spectra of complex bursts can likely be fitted in the same way. Moreover, BD14 actually explored in detail how the observed emission of a single pulse depends on the various physical parameters of the internal shock model. Their study shows that the assumptions about the dynamics (Lorentz factor, kinetic energy flux, etc.) affect the pulse light curve but have little effect on the shape of the spectrum.

4. Spectral analysis of the synthetic bursts

We first focused our study of the three synthetic bursts in the GBM energy range (8 keV to 40 MeV). The four phenomenological functions and the ISSM function were used to fit the spectra of the synthetic bursts in the four time intervals [0 s, 1 s], [1 s, 3 s], [3 s, 6 s] and [0 s, 6 s] using the *XSPEC* software. The reference energy E_0 in Eqs. 4, 6 and 7 was fixed to 500 keV. For simplicity, the reference energy in Eq. 13, which relates to the flux normalization, was fixed to the true peak energy of the synthetic spectra: $E_r = 1150, 478, 114$ and 745 keV for the time intervals [0 s, 1 s], [1 s, 3 s], [3 s, 6 s] and [0 s, 6 s], respectively. To compare the quality of the fits between the different functions, we defined the following quality factor Q that mimicks a reduced χ^2 :

$$Q = \frac{1}{n - n_{\text{par}}} \sum_{i=1}^n \left(\frac{\Gamma(E_i) - s(E_i)}{\sigma_i} \right)^2 \quad (16)$$

where $\Gamma(E_i)$ is the local photon index of the fitted function and $s(E_i)$ is the true index of the synthetic spectrum at energy E_i . The error σ_i on $\Gamma(E_i)$ is obtained by propagating the errors of the n_{par} fitted function parameters.

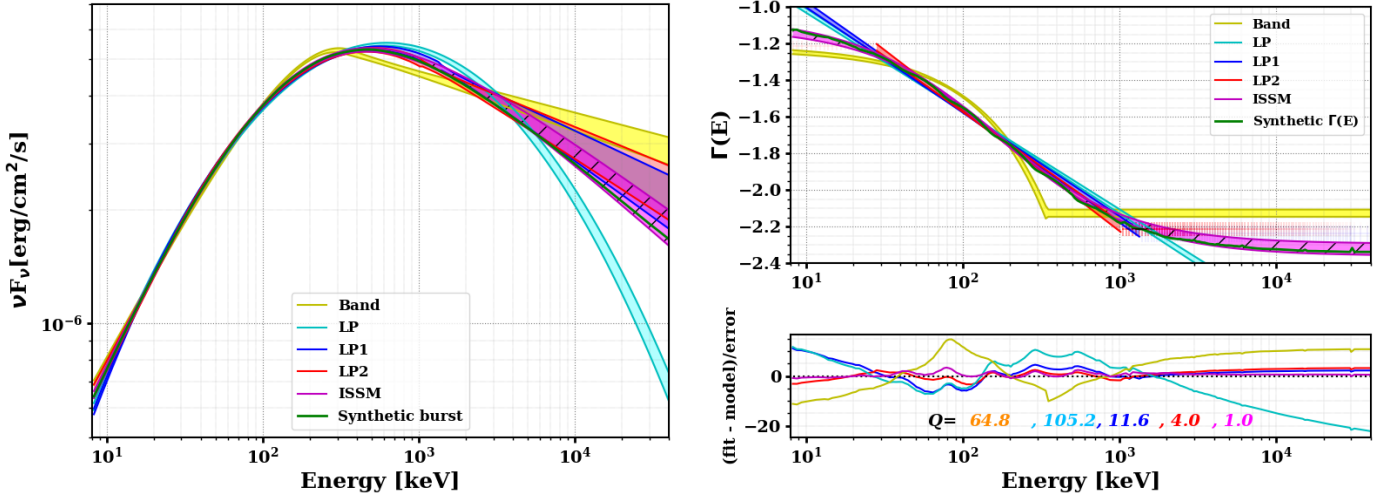
The spectral analyses were performed using the Castor fit statistic⁴ (C_{stat}) for Poisson distributed total counts of the burst. The C_{stat} values obtained from the fits of the three synthetic burst spectra are reported in Table 1. The ISSM function has the lowest C_{stat} value in most of the time intervals especially for the synthetic burst with the highest flux value i.e. GRB_B001. For GRB_B100, all functions yield similar C_{stat} values, meaning that the fits are of similar quality owing to the low photon statistics for this faint burst. Fig. 3 shows the SEDs and local photon index of the GRB_B010 burst in the time interval [1 s, 3 s], as obtained from the fits with the five spectral functions. As can be seen from this figure, both the SED and the local photon index are not reproduced by the Band function fit, in particular around and above the peak energy. The fit quality of the LP function is even worse owing to the linear dependency of its local photon index with energy, which is not adequate at low and high energies. The LP1 and LP2 functions provide better fits and their parameters are not constrained for the three bursts in all the time intervals. Finally, Fig. 3 shows that the ISSM function has the lowest Q value among all fitted functions, which is expected from this model that has been built directly from the synthetic spectra.

By nature, the ISSM function reproduces the keV-MeV spectra of the synthetic bursts simulated with the internal shock synchrotron model. It has the same number of free parameters as the Band function, which is commonly used to fit the prompt high-energy spectrum of GRBs. Therefore, before applying these functions to real GRB observations (see Sect. 5), it is worth comparing their shapes in detail. Tables A.1, A.2, and A.3 in appendix show the parameters of the Band and ISSM fits to GRB_B001, GRB_B010 and GRB_B100, respectively. The asymptotic low-energy index α of the ISSM function is found to be larger than that of the Band function, while the high-energy index β is smaller. Interestingly, the peak energies of the synthetic bursts are estimated

⁴ See <https://heasarc.nasa.gov/docs/xanadu/xspec/xspec11/manual/node57.html>.

Table 1. C_{stat} values of the spectral fits of the three synthetic bursts, performed with the five functions: Band, LP, LP1, LP2 and ISSM.

Synthetic GRB	Model	DOF	C_{stat} for time intervals:			
			[0-1] s	[1-3] s	[3-6] s	[0-6] s
GRB_B001	Band	473	603	906	486	1403
	LP	474	768	677	615	631
	LP1	473	768	569	615	589
	LP2	472	526	540	558	570
	ISSM	473	486	498	452	638
GRB_B010	Band	473	458	539	447	578
	LP	474	470	559	455	469
	LP1	473	470	534	455	469
	LP2	472	439	525	455	466
	ISSM	473	441	523	443	484
GRB_B100	Band	473	465	446	359	461
	LP	474	464	445	364	447
	LP1	473	464	445	364	447
	LP2	472	462	442	376	447
	ISSM	473	463	444	360	449


Fig. 3. Left: SEDs of the GRB_B010 synthetic burst in the time interval [1 s, 3 s], from fits with the five spectral functions. The fit with the ISSM function is presented by the hatched magenta line. Right: Local photon index as a function of the photon energy. The fit quality factor Q of the five functions is given in the bottom panel.

with much greater accuracy with the ISSM function than with the Band function, which underestimates them by $\sim 36\%$. Furthermore, we compared the spectral width of the two functions, following Yu et al. (2015) who proposed a method to calculate the SED sharpness around its peak energy. We did not consider the alternate measure of the spectral width proposed by Axelsson & Borgonovo (2015), which is defined as $W = \log(E_2/E_1)$ where E_1 and E_2 are the energy bounds of the SED full width at half maximum. The spectral sharpness angle defined by Yu et al. (2015) is computed from the triangle defined by the vertices at $E_p/10$, E_p and $3E_p$. To compute this angle and its asymmetrical errors accurately, we performed Monte-Carlo simulations using the fit parameters and their covariance matrix, assuming that their distribution is a multivariate Gaussian. This process was repeated 1000 times for each time interval and for each of the two bright synthetic bursts GRB_B001 and GRB_B010. The spectral sharpness angle was chosen as the maximum probability value (MPV) of the distribution obtained from the 1000 realizations. The errors on the angle were calculated from the 68% confidence intervals on each side of the MPV. The results of this analysis are reported in Table 2, which confirms that the ISSM function reproduces the spectral width of the synthetic bursts better than the Band function.

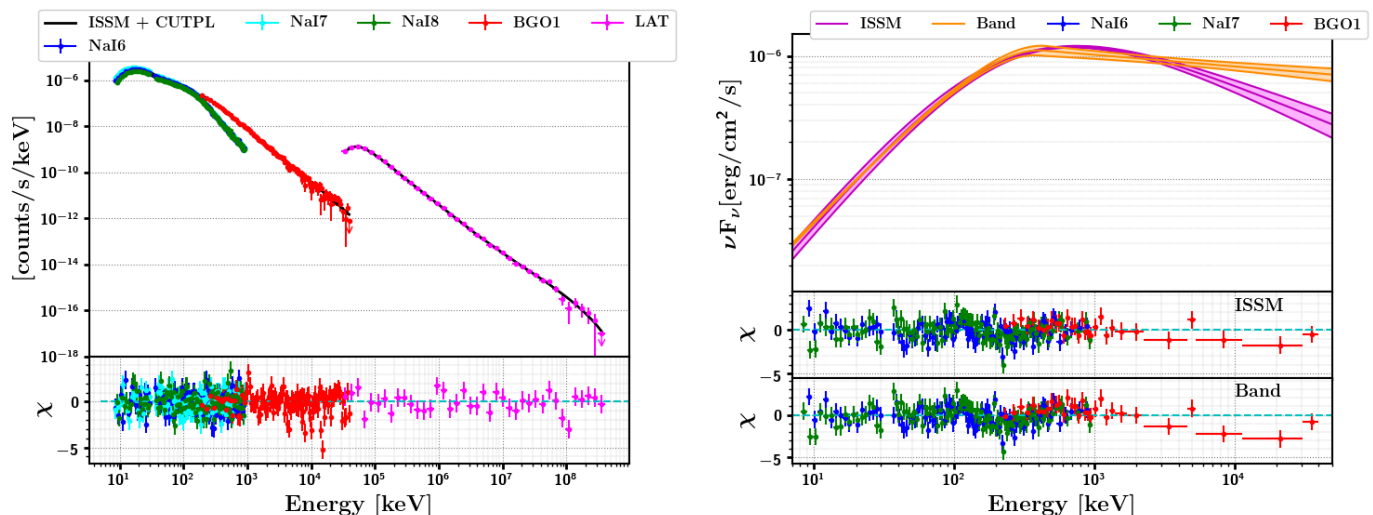
For the sake of completeness, we carried out broadband spectral analyses of the brightest synthetic burst (GRB_B001) in the two time intervals [1 s - 3 s] and [3 s - 6 s], where the inverse Compton spectral component is prominent. We used the CUTPL model to fit this high-energy spectral component and fixed the reference energy E_0 to 10 GeV in Eq. 8. This value is close to the decorrelation energy and thus minimizes the correlation between the CUTPL parameters. Despite its brightness in the LAT energy range, the inverse Compton component of GRB_B001 peaks at ~ 100 GeV, where few simulated events are recorded. We multiplied artificially the LAT effective detection area by 100 to get rid of these statistical limitations and to check whether the adopted model is able to capture all features in the internal shock model spectra. The fit results obtained with the ISSM + CUTPL model in the two time intervals are reported in Table 3 and shown in the left panel of Fig. 4 for the time interval [1 s - 3 s]. The fit residuals

Table 2. Spectral sharpness angle (in degrees) from the Band and ISSM fits to the synthetic bursts GRB_B001 and GRB_B010.

Synthetic GRB	Model	Time interval			
		[0-1] s	[1-3] s	[3-6] s	[0-6] s
GRB_B001	Synthetic	142.3	145.9	145.5	148.9
	Band	137.7 ^{+0.4} _{-0.2}	140.0 ^{+0.2} _{-0.1}	142.7 ^{+0.6} _{-0.3}	142.0 ^{+0.2} _{-0.1}
	ISSM	143.5 ^{+0.5} _{-0.5}	145.7 ^{+0.3} _{-0.3}	145.8 ^{+1.0} _{-1.0}	148.6 ^{+0.4} _{-0.3}
GRB_B010	Synthetic	142.3	145.9	145.5	148.9
	Band	139.1 ^{+0.9} _{-1.2}	139.9 ^{+0.7} _{-0.4}	145.1 ^{+1.8} _{-1.4}	142.6 ^{+0.4} _{-0.6}
	ISSM	143.6 ^{+1.8} _{-1.3}	146.5 ^{+1.1} _{-1.2}	150.6 ^{+4.7} _{-4.7}	148.9 ^{+1.3} _{-0.8}

Table 3. Results of the ISSM + CUTPL fits to the synthetic burst GRB_B001 during the time intervals [1 s - 3 s] and [3 s - 6 s].

Spectral component	Fit results	Time interval	
		[1-3] s	[3-6] s
ISSM	E_p (keV)	458 ± 4	119 ± 3
	α	-1.09 ± 0.01	-1.03 ± 0.05
	β	-2.354 ± 0.003	-2.321 ± 0.004
	A_{MeV} (keV ⁻¹ cm ⁻² s ⁻¹)	0.145 ± 0.001	0.193 ± 0.001
CUTPL	λ	-1.51 ± 0.06	-1.28 ± 0.07
	E_f (GeV)	165 ± 71	172 ± 91
	A_{GeV} (keV ⁻¹ cm ⁻² s ⁻¹)	(167.4 ± 11.5) × 10 ⁻¹³	(39.0 ± 3.5) × 10 ⁻¹³
ISSM + CUTPL	C_{stat}/DOF	533/510	502/510

Fig. 4. Left: Fit of the count spectrum of the synthetic burst GRB_B001 with the ISSM + CUTPL model in the time interval [1 s - 3 s]. Right: Fit of the ISSM and Band models to the GRB 150403913 spectrum observed by the GBM.


and reduced C_{stat} values clearly show the excellent quality of the fits and the ability of the ISSM + CUTPL model to reproduce the broadband shape of the synthetic spectra.

5. Application to GBM bursts

5.1. GRB sample and data selection

According to the results presented in Sect. 4, a large number of counts is required to distinguish the different spectral model based on their fit quality. For this reason, we selected a sample of bursts detected by the GBM with an energy fluence larger than 10⁻⁵ erg cm⁻² (from 10 to 1000 keV), namely comparable to those of the GRB_B001 and GRB_B010 synthetic bursts. Like in Sect. 4, we first focused our study on the sub-MeV spectral component, discarding the bursts that have additional components at low or high energies. This includes the GRBs with a low-energy excess that has been interpreted as a possible thermal component (GRB 090424, GRB 090820 (Tierney et al. 2013), GRB 090902B (Abdo et al. 2009), GRB 090926A (Guiriec et al. 2015), GRB 100724B (Guiriec et al. 2011), GRB 110721 (Axelsson et al. 2012)), the GRBs with an extra high-energy power-law component (GRB 080916C (Ackermann et al. 2013), GRB 090902B (Abdo et al. 2009), GRB 090926A (Ackermann et al. 2011)) or with a strong spectral evolution (GRB 081215A (Tierney et al. 2013)). The bursts whose spectra are best fitted by a simple power law in the GBM spectral

catalog⁵ (Gruber et al. 2014) were also excluded. Beside these 15 GRBs, we eliminated the bursts which have been seen by NaI detectors with a separation angle between the detector axis and the source larger than 60°. As a result, we selected 74 GBM GRBs in the first eight observing years, which are listed in Table A.4 in appendix. More than half of them (41) are best fitted by the Band function in the GBM spectral catalog (Gruber et al. 2014). Another fair fraction of bursts from this catalog (24) are best fitted by a power law with an exponential cutoff. This model is a special case of the Band function that is obtained for a very steep high-energy index (i.e., β tends to $-\infty$ and E_b to $+\infty$ in Eq. 2). The remaining 9 GRBs were found to be best fitted by a smoothly broken power law by Gruber et al. (2014), which is characterized by a flexible SED width around its peak energy. The data are loaded from the FSSC GBM data⁶ using `gtburst` tool⁷. The spectral analyses were performed during the T90 defined in GBM catalog Gruber et al. (2014). For each GRB of the sample, we selected one BGO detector with a separation angle less than 90° and a maximum of three NaI detectors that have seen the burst with a separation angle less than 60°.

5.2. Model comparison

We performed a spectral analysis of the 74 selected GRBs with the *XSPEC* software and for the five spectral models: Band, LP, LP1, LP2 and ISSM. The reference energies E_0 in Eqs. 4, 6, 7 and E_r in Eq. 13 of the LP, LP1, LP2 and ISSM functions, were fixed to 500 keV. We used the ‘‘Poisson-Gauss’’ fit statistic⁸ (PG_{stat} hereafter), which is suitable for GRB spectral analysis, where the observed data counts are Poisson distributed in the energy channels, while background counts have been estimated beforehand from pre- and post-burst data and are assumed to follow a Gaussian distribution. The case of GRB 150403913 is shown in the right panel of Fig. 4 for the ISSM and Band fits. The left panel of Fig. 5 shows the increase of PG_{stat} of the five models with respect to the model which has the lowest PG_{stat} (‘‘reference model’’ hereafter). In this panel, the GRBs are displayed in order of increasing signal-to-noise ratio (SNR), which is defined for each GRB as:

$$\text{SNR} = \frac{\sum_{i=1}^N (c_i - b_i)}{\sqrt{\sum_{i=1}^N b_i}} \quad (17)$$

where c_i (resp. b_i) are the total (resp. background) counts recorded by the N NaI detectors that have detected the burst. The right panel of Fig. 5 shows the resulting distribution of ΔPG_{stat} for the five models. The ISSM function has the lowest PG_{stat} , namely it is the reference model, for half of the GRBs in Fig. 5. Since the ISSM function shows the lowest value of PG_{stat} in half of the cases, it is taken as a reference (level 0 on the bottom of Fig. 5) and the other models are displayed accordingly. The first GRBs with the minimum SNR values in this figure have comparable PG_{stat} values for the five spectral models and the ΔPG_{stat} increases with SNR as expected, since the models can be more easily distinguished from each other with a larger event statistics.

To compare the fitted models with each other, we used the ΔPG_{stat} as a likelihood ratio test (Neyman & Pearson 1928). In case of nested models, where the model parameterization in the null hypothesis is a special case of that in the alternative hypothesis, the ΔPG_{stat} is expected to follow a χ^2 distribution with k degrees of freedom in the large sample limit, where k is the number of additional parameters between the two models (Wilks 1938). Since several of the models that we considered are not nested, and because the large sample limit is not reached in all energy channels of the GRBs in our sample, one should compute the ΔPG_{stat} probability density function for each GRB and each pair of models by simulating a large number of spectra. Given the vast number of cases, we focused on the Band and ISSM functions, in the two cases of a low or a medium value of the SNR. We performed Monte-Carlo simulations for two cases in our sample, GRB 100910A (SNR=141) and GRB 110921A (SNR=249), considering the Band function as the null hypothesis. We used the *XSPEC* software to simulate 10^5 Band spectra for the duration of each GRB, using the DRM and background files of the GBM detectors that have seen the burst with the best viewing angle. All the simulated spectra were then fitted with the Band and ISSM functions. The resulting distribution of $\Delta PG_{\text{stat}} = PG_{\text{stat, Band}} - PG_{\text{stat, ISSM}}$ for GRB 110921A is shown in the left panel of Fig. 6. The fit of this distribution with an asymmetric Gaussian function and its extrapolation allowed us to compute the ΔPG_{stat} limit beyond which the probability that a statistical fluctuation yields a better fit with the ISSM function than with the Band function is smaller than 10^{-6} (approximately 5 Gaussian standard deviations). The limit was found to be $\Delta PG_{\text{stat}} = 20$ for a low SNR and 3 for a medium SNR, beyond which the null hypothesis (i.e., the Band function) must be rejected. Because it was complicated and time consuming to determine a limit for each GRB and each pair of models, we adopted a common limit of $\Delta PG_{\text{stat}} = 10$ in all situations.

As a result, this study revealed that the ISSM model is the reference model for 36 GRBs, 19 of which are equivalently fitted by the Band function. On the contrary, the Band function has the lowest PG_{stat} value for 16 GRBs, 10 of which are equivalently fitted by the ISSM function. Concerning the other three models, only the LP2 showed good performance. It is the reference model for 18 GRBs, and globally as good as the Band model, though with one more parameter. All in all, the ISSM function is a good spectral model for 81% (60/74) of the GRBs in our sample, namely in these cases it is the reference model or it is close enough to it in terms of PG_{stat} . The Band function was found to be a good spectral model for a smaller fraction (59%) of the GRB sample (44/74), similar to the LP2 function (65%), versus only $\sim 20\%$ for the LP1 and LP functions. It must be noted that these performances would improve for more common and less fluent bursts with lower signal-to-noise ratios.

⁵ <https://heasarc.gsfc.nasa.gov/W3Browse/fermi/fermigbrst.html>

⁶ <https://fermi.gsfc.nasa.gov/ssc/data/access/gbm/>

⁷ <https://fermi.gsfc.nasa.gov/ssc/data/analysis/scitools/gtburst.html>

⁸ See <https://heasarc.gsfc.nasa.gov/xanadu/xspec/manual/XSappendixStatistics.html>

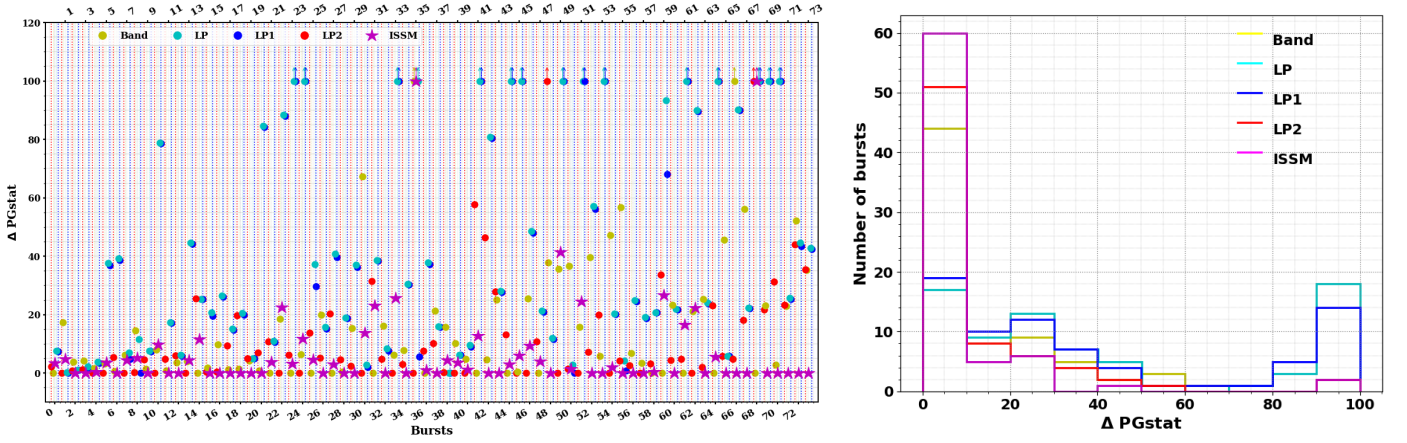


Fig. 5. Left: Difference in PG_{stat} of the five models with respect to the model with the lowest PG_{stat} , for every GRB displayed with increasing SNR (increasing from the left to the right). For each GRB, the five model markers are displayed within two vertical (red and blue) lines. By definition, the model with the lowest PG_{stat} is always placed on the zero horizontal line. Lower limits at the top of the figure stand for models with a ΔPG_{stat} larger than 100. Right: Distribution of ΔPG_{stat} for the five models.

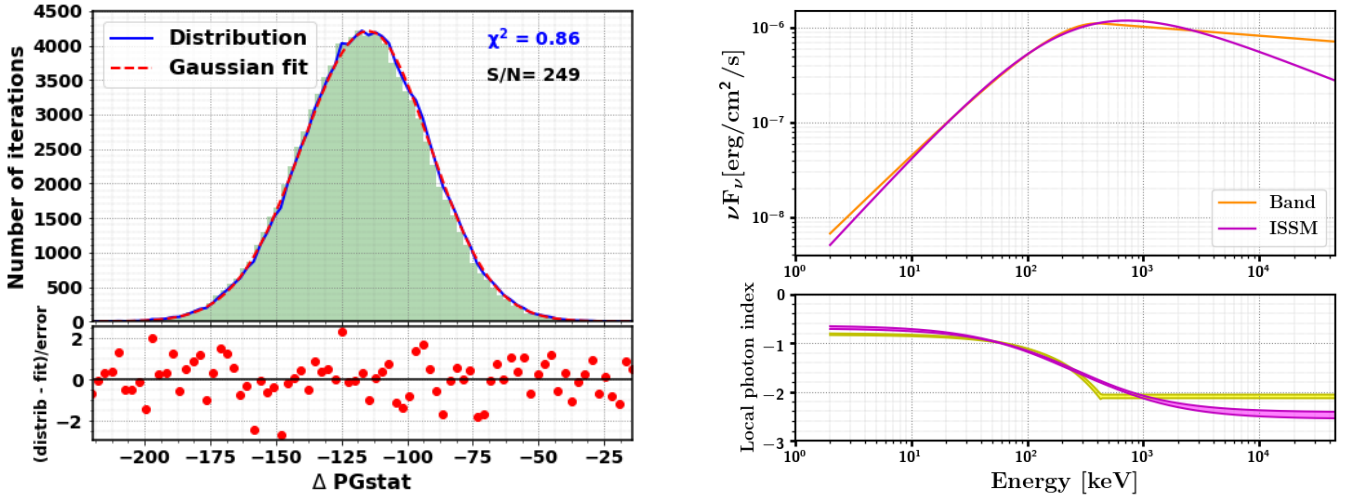


Fig. 6. Left: Fit of an asymmetric Gaussian function to the distribution of ΔPG_{stat} between the Band and the ISSM function for the medium SNR case. The bottom panel shows the ratio of the difference between the histogram and its fit over the error (\sqrt{N} in each bin). Right: Spectral energy distribution and local photon index of a representative burst (GRB 150403913) with the Band and ISSM functions.

5.3. Band and ISSM spectral parameters

In this section we compare the spectral parameters of the Band and ISSM functions. The left panel of Fig. 7 shows the SED peak energies obtained with the two models. The E_p values of the ISSM function are found to be systematically larger than the values obtained with the Band function. The low-energy index α is an asymptotic value that is rarely reached by the local photon index within the energy range of any burst-observing instrument. For this reason, Preece et al. (1998) defined an effective low-energy index at the CGRO/BATSE detector lower limit (25 keV). In order to find the energy limit (E_{lim}) at which the local photon index $\Gamma(E)$ approaches the asymptotic value α within its error $\delta\alpha$, we solved the equation $\Gamma(E_{\text{lim}}) = \alpha - \delta\alpha$ using the definition of the local photon index of the Band and ISSM functions in Eqs. 3 and 15, respectively. The E_{lim} energies of the two functions are expressed as:

$$E_{\text{lim,Band}} = \frac{\delta\alpha}{2 + \alpha} E_p \quad (18)$$

$$E_{\text{lim,ISSM}} = \frac{\delta\alpha(2 + \beta)}{(2 + \alpha)(\beta - \alpha + \delta\alpha)} E_p \quad (19)$$

These quantities are displayed with respect to E_p in the right panel of Fig. 7. For the vast majority of the GRBs in our sample, the E_{lim} values fall below the GBM energy range. We thus defined α_{10} as the local photon index at 10 keV, namely right above

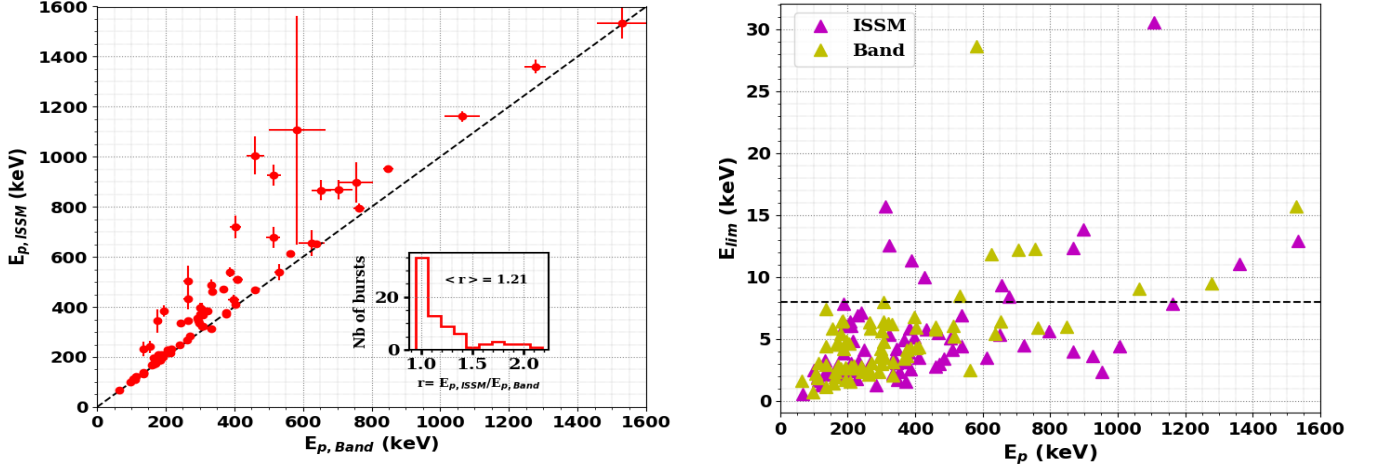


Fig. 7. Left: Comparison of the E_p parameter between the Band and ISSM functions. The dashed line is the equality line. The inset shows the ratio between the E_p values obtained by ISSM and Band functions. Right: limit energies E_{lim} of the ISSM and Band functions compared with their peak energies E_p . The horizontal dashed line represents the lower limit of the GBM energy range.

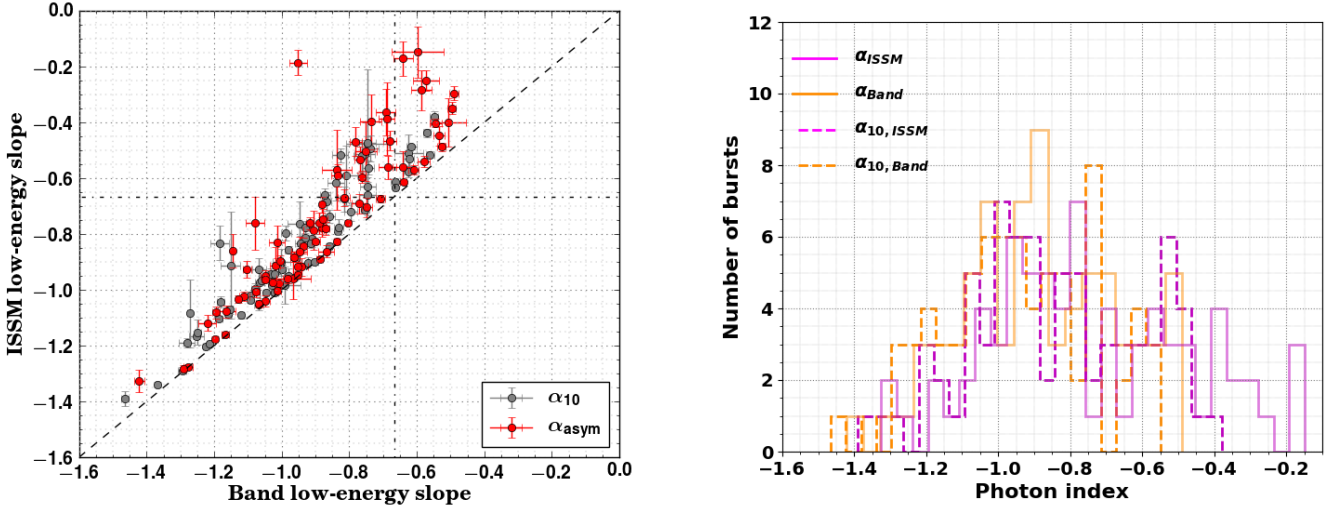


Fig. 8. Left: Comparison of the asymptotic α and the local photon index α_{10} at 10 keV between the Band and ISSM functions. The gray dashed line denotes equality. The dashed-dotted horizontal and vertical lines indicate the upper limit ($-2/3$) of the low-energy spectral index for synchrotron emission in the slow cooling regime. Right: Distributions of the α and α_{10} parameters of the Band and ISSM functions.

the low-energy detection limit of the GBM. The left panel of Fig. 8 compares the α_{10} index to the α asymptotic index for both the Band and ISSM functions. While the α indices of the ISSM function are larger than those of the Band function, the α_{10} indices of the ISSM function are only slightly larger. The values of α_{10} appear also less scattered than those of α . More interestingly, the fraction of GRBs that are fitted with the ISSM function and whose index is harder than the synchrotron slow-cooling limit ($-2/3$) decreases from 35% (α asymptotic index) to 26% (α_{10}). This fraction decreases from 19% to 12% for the Band function. As shown in the right panel of Fig. 8 that displays the α and α_{10} distributions for both models, the weighted mean index of the ISSM (resp. Band) function indeed decreased from $\langle \alpha \rangle = -0.75$ (resp. -0.88) to $\langle \alpha_{10} \rangle = -0.97$ (resp. -1.03).

Similarly, the β parameter of the ISSM function is an asymptotic value at high energy, which may not be reached by the local photon index within the GBM energy range. Therefore, we defined β_b as the photon index at the break energy E_b of the Band function (Eq. 2). By definition, β_b is equal to β for the Band function, while it is harder than β for the ISSM function owing to its continuous curvature. The β_b index of the ISSM function was also found to be systematically harder than that of the Band function, namely $\beta_{ISSM} < \beta_{Band} < \beta_{b,ISSM}$. As a result, GRB spectra appear slightly wider around their peak energy when fitted with the ISSM function than with the Band function, but narrower when observed over a wider energy range. This is illustrated in the right panel of Fig. 6, for the case of GRB 150403913, which is best fitted by the ISSM model.

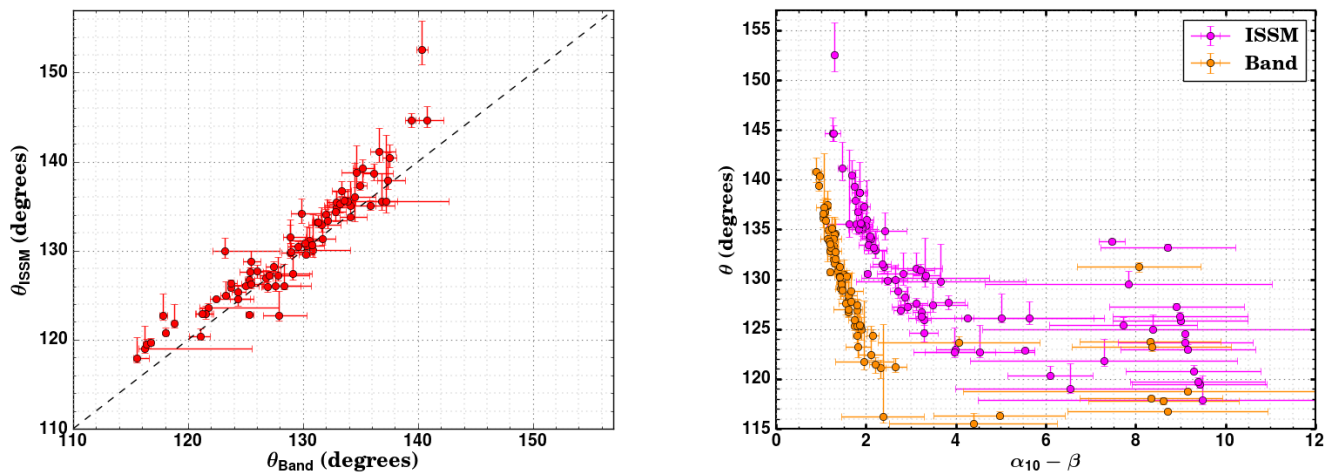


Fig. 9. Left: Spectral sharpness angles of the ISSM fits versus the angles of the Band fits to the GRB spectra. Right: Spectral sharpness angle as function of the difference between the α_{10} and β parameters for the Band and ISSM functions.

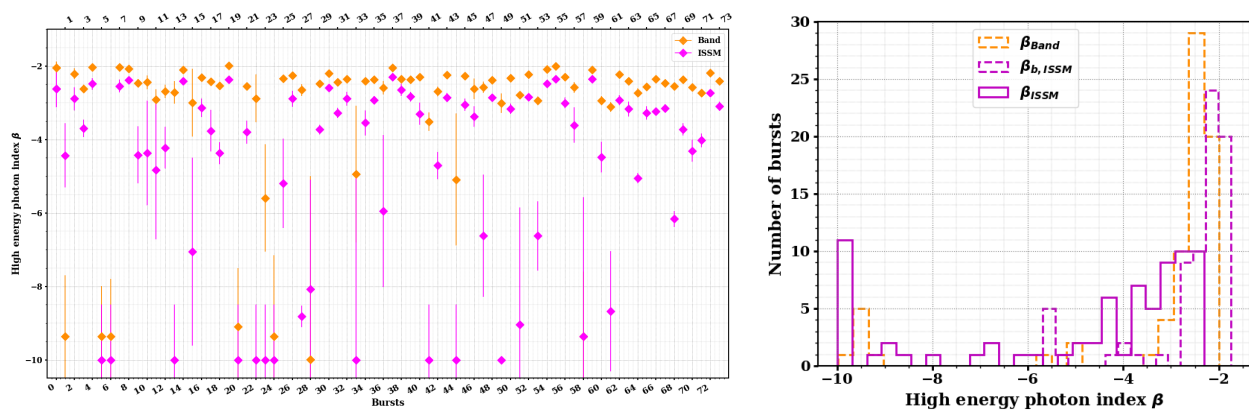


Fig. 10. Left: Distribution of the high-energy index β of the Band and ISSM functions. The lowest limit value used for β was fixed to -10. Right: Distributions of the β parameter of the Band and ISSM functions.

5.4. Band and ISSM spectral sharpness

We investigated how the sharpness of the Band and ISSM fitted spectra varies quantitatively with the photon indices. Following the methodology described in Sect. 4, a set of 10^3 spectra was simulated for each GRB using its fit parameters and their covariance matrix. The spectral sharpness angles of the GRB sample are presented in the left panel of Fig. 9. Similarly to the synthetic bursts analyzed in Sect. 4, the ISSM spectra are slightly wider than the Band spectra. As expected, the spectral sharpness angle was found to be independent of the peak energy, and to depend strongly on the photon indices. As shown in the right panel of Fig. 9, the spectral sharpness angle decreases with increasing α_{10} and/or with decreasing β . The spectral sharpness angles of the GRBs in our sample are similar to those obtained by Yu et al. (2015) (see figures therein, e.g., the blue solid curve in the left panel of Fig. 7), ranging from $\sim 115^\circ$ to $\sim 140^\circ$ in both analyses, except one with angle 152° with the ISSM function.

More importantly, the spectral sharpness angle of the synthetic bursts fitted by the ISSM function is 149° (see Table 2), which is larger than for any GRB in our sample using the same fitting model. This results essentially from the difference in the low-energy spectral index, $\alpha \simeq -1.2$, which is softer than for most of the analyzed GRBs (see the left panel of Fig. 8). Besides, the value of the high-energy index of the synthetic burst, $\beta \simeq -2.3$, is close to the higher bound of the sample distribution as shown in Fig. 10. Possible ways to improve the agreement between the synthetic and observed bursts will be discussed in Sect. 7.

6. Application to GRB 090926A

The prompt light curve of GRB 090926A shows a short and bright spike at 10 s post-trigger which has been detected from keV to GeV energies by the *Fermi* instruments (Ackermann et al. 2011). This spike coincides with the emergence of a hard power-law spectral component which is attenuated at the highest energies. In Y17, we performed a dedicated analysis of the broadband prompt emission spectrum of GRB 090926A by combining the GBM data with the LAT Pass 8 data above 30 MeV. Using a Band +CUTBPL fitting function, we showed that the spectral break energy increases with time, and that the entire prompt emission of this burst,

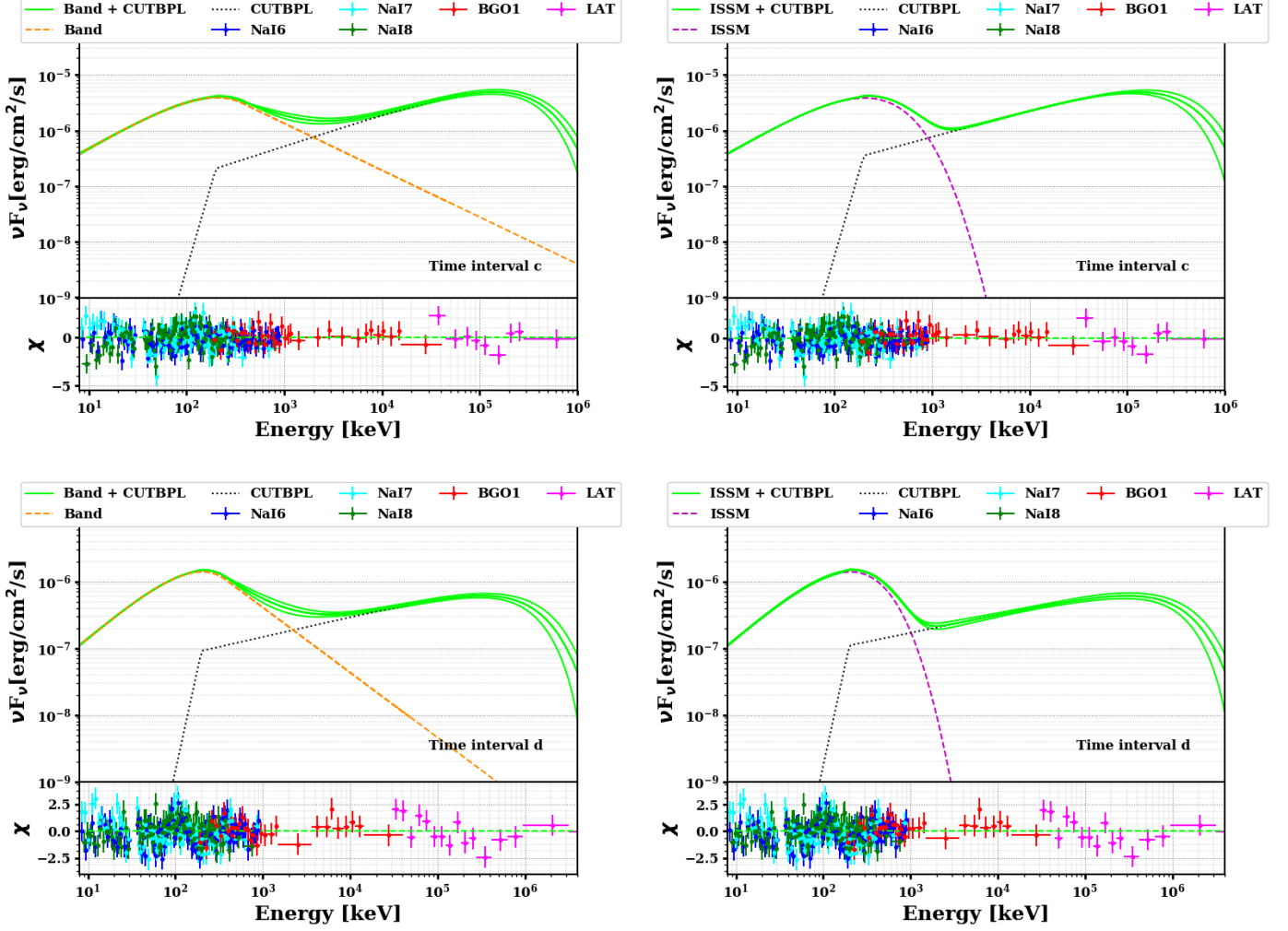


Fig. 11. Spectral energy distributions of GRB 090926A in time intervals *c* (top panels) and *d* (lower panels) from the joint GBM/LAT analysis using LAT Pass 8 above 30 MeV. The solid curve represents the Band + CUTBPL model (left column) and the ISSM + CUTBPL model (right column), within a 68% confidence level contour derived from the errors on the fit parameters. The reference energy of the CUTBPL was fixed to 10 MeV like in Y17.

namely the emission that is observed from keV to GeV energies by the GBM and the LAT during the GRB duration in the 50–300 keV energy band, can be interpreted as the result of synchrotron emission of shock-accelerated electrons in the keV–MeV domain, with an inverse Compton spectral component at higher energies. The latter component was fitted by the CUTBPL function instead of the CUTPL function to avoid any unrealistic contribution to the observed flux in the GBM low-energy range. As a result, the low-energy index α of the Band spectral component was found to be close to -0.9 , which is in agreement with the theoretical index (~ -1) of the fast-cooling synchrotron spectrum that is expected in the presence of inverse Compton scatterings in the Klein-Nishina regime (BD14).

Going further, we revisited the spectral analysis of GRB 090926A and compared the Band + CUTBPL model to the ISSM + CUTBPL model. This analysis was performed with the *XSPEC* software for the time intervals *c* (0.98 s to 10.5 s) and *d* (10.5 s to 21.5 s) where the high-energy break is detected. Following Y17, we fixed the parameters γ_0 and the break energy E_b of Eq. 9 to +4 and 200 keV, respectively. Like in Y17, the reference energy E_0 was fixed to 10 MeV and 100 MeV for the time intervals *c* and *d*, respectively. The results of this analysis are presented in Fig. 11 and summarized in Table 4. As can be seen in all panels of this figure and from the PG_{stat} fit statistics, both the Band + CUTBPL and ISSM + CUTBPL models reproduce adequately the GRB spectrum, especially in the time interval *c* (top panels). The low-energy indices α of the Band and ISSM spectral components are equal within statistical errors, and close to -1 and -0.9 for the time intervals *c* and *d*, respectively. Again, these values perfectly agree with the predictions of BD14. All other spectral parameters are also equivalent between both models, except the high-energy index β of the keV–MeV spectral component, which is not well constrained using the ISSM function. Since the ISSM flux decreases more rapidly than that of the Band function beyond the SED peak energy, this likely results from the lack of photon statistics in the SED dip at a few MeV, between the GBM and LAT energy domains.

Table 4. Results of the Band +CUTPL and ISSM +CUTBPL fits to GBM/LAT data in the time intervals c and d of GRB 090926A.

Time intervals	Parameters	Band + CUTBPL	ISSM + CUTBPL
[0.98 s - 10.5 s]	$A_{\text{Band/ISSM}}$ ($\text{keV}^{-1} \text{cm}^{-2} \text{s}^{-1}$)	$0.33^{+0.02}_{-0.01}$	$580^{+5}_{-5}(\times 10^{-5})$
	E_p (keV)	203^{+7}_{-7}	203^{+1}_{-1}
	α	$-0.98^{+0.03}_{-0.03}$	$-0.97^{+0.02}_{-0.02}$
	β	$-2.8^{+0.2}_{-0.3}$	$-14.0^{+4.7}_{-1.0}$
	A_{CUTBPL} ($\times 10^4 \text{keV}^{-1} \text{cm}^{-2} \text{s}^{-1}$)	$2.04^{+1.37}_{-0.89}$	$3.46^{+0.22}_{-0.32}$
	λ	$-1.43^{+0.10}_{-0.11}$	$-1.52^{+0.02}_{-0.02}$
	E_f (GeV)	$0.25^{+0.07}_{-0.05}$	$0.27^{+0.07}_{-0.05}$
	$PG_{\text{stat/DOF}}$	577/510	582/510
[10.5 s - 21.5 s]	$A_{\text{Band/ISSM}}$ ($\text{keV}^{-1} \text{cm}^{-2} \text{s}^{-1}$)	$0.123^{+0.003}_{-0.003}$	$203^{+16}_{-11}(\times 10^{-5})$
	E_p (keV)	201^{+5}_{-5}	204^{+7}_{-5}
	α	$-0.88^{+0.02}_{-0.02}$	$-0.86^{+0.02}_{-0.02}$
	β	$-3.0^{+0.1}_{-0.3}$	-14^{+9}_{-1}
	A_{CUTBPL} ($\times 10^7 \text{keV}^{-1} \text{cm}^{-2} \text{s}^{-1}$)	$8.89^{+2.92}_{-2.72}$	$10.74^{+1.65}_{-2.93}$
	λ	$-1.70^{+0.06}_{-0.05}$	$-1.73^{+0.05}_{-0.04}$
	E_f (GeV)	$1.08^{+0.31}_{-0.25}$	$1.12^{+0.32}_{-0.25}$
	$PG_{\text{stat/DOF}}$	714/510	717/510

7. Discussion

Our analysis of a sample of 74 GRBs that are bright and fluent in the GBM showed that the ISSM function adequately reproduces most (81%) of the keV-MeV prompt emission spectra, while the Band phenomenological function is suitable for a smaller fraction (59%). We observed noticeable differences between the spectra fitted with these two functions. The peak energies E_p of the spectra that are reconstructed using the ISSM function are somewhat higher than those of the spectra resulting from the Band function fits. In addition, the ISSM fitted spectra are globally narrower than the Band fitted spectra, yet they appear slightly wider close to E_p . This results in slightly larger sharpness angles for the ISSM fitted spectra, which was also observed from fits of the synthetic spectrum.

Although the shape of the ISSM function seems adequate to reproduce the spectral curvature of the GBM bright bursts, the spectral sharpness angle in this sample is always smaller than the sharpness angle of the synthetic spectra that were used to build this fitting function. Since the spectral sharpness angle scales almost linearly with $\beta - \alpha$ (right panel of Fig. 9), it is worth investigating possible ways to improve the agreement between the data and the physical model. Firstly, the high-energy photon index β in the model is strongly related to the slope of the electron power-law energy distribution p , as $\beta = -(p/2 + 1)$ in the synchrotron fast-cooling regime. While $p = 2.7$ and thus $\beta = -2.3$ for the synthetic bursts, larger values of p up to 2.9 could be considered (BD14), owing to the theoretical uncertainties on the energy distribution of accelerated electrons in mildly-relativistic shocks. However, the expected change in the value of β would not entirely account for the sharpness discrepancy with observed spectra. Moreover, many of the observed values of β are larger for the bursts with well-measured spectral parameters as shown in Fig. 10. In this figure, softer high-energy indices appear with larger uncertainties and might be underestimated due to insufficient photon statistics above the peak energy. This suggests that a better spectral coverage at MeV energies could result in harder values of β and in larger sharpness angles for this fraction of the burst sample, making the entire sample compatible with the physical model.

Secondly, the low-energy photon index α of the synthetic spectra is close to -1.2 . As shown in Fig. 9, an increase of 0.5 in this theoretical slope, with a condition that the high-energy slope does not increase, would be enough to make the synthetic spectra compatible with the GBM sample in terms of spectral sharpness. As a matter of fact, harder values of α are expected from internal shock synchrotron models in the so-called marginally fast-cooling regime (Daigne et al. 2011; Beniamini & Piran 2013), where the impact of adiabatic losses on the electron energy distribution is not negligible anymore as compared to the effect of radiative losses. In this regime, specific configurations of the jet such as low-contrast internal shocks can lead to α values as hard as $-2/3$ (Daigne et al. 2011). Hardening the low-energy part of the synchrotron spectrum could also be obtained by accounting for the decay of the magnetic field behind the shock (Pe'er & Zhang 2006; Derishev 2007). In such a configuration, the most energetic electrons would indeed explore a small region where the magnetic field has not decreased yet, while the less energetic electrons would see a less intense magnetic field on average. Therefore, such a magnetic field decay appears as a natural possibility to reach the marginally fast cooling regime without any need for a fine-tuning of the microphysical parameters (Daigne & Bošnjak, in preparation). Indeed, as the magnetic field decreases, the critical Lorentz factor of electrons for slow cooling γ_c increases.

Preliminary results show that a steep asymptotic slope α close to $-2/3$ is obtained. This effect of a magnetic field decay is shown in the right panel of Fig. 2 where the value of the ISSM low-energy slope $\alpha = b/c - a$ varies between -1.5 (case A with a constant magnetic field) and -0.8 (case B with a magnetic field decay for the spectrum measured at the peak of the light curve). This illustrates that a more realistic modeling of the microphysics in the acceleration and emission regions should be investigated to reach a full agreement between the synthetic and observed spectra. Ultimately one would like to use the spectral fits to infer the physical parameters of the model such as the evolution of the injected power or the distribution of the Lorentz factor in the flow. In practice, analysis of the spectra only provides values for the four parameters: A_{ISSM} , α , β and E_p . They partially constrain the shock physics and radiative mechanism as discussed above for α and β . The peak energy E_p depends on a combination of the ejecta physical parameters and shock microphysics. It will therefore be difficult to decipher from the evolution of E_p the form of the Lorentz factor or/and injected power distributions even if some general trends can probably be obtained. This will require a dedicated study.

8. Conclusions

The physical origin of GRB prompt emission remains elusive despite decades of observations. Characterizing the prompt emission spectra has been often performed using phenomenological parameterizations with little physical grounds, such as the Band function. However, the advance of instrument spectral coverage and the improved data quality provided by current missions such as the *Fermi* observatory now offer the possibility to confront observations to theoretical models in detail. In this work, we used the internal shock model developed by BD14 to produce synthetic GRBs (see also Bošnjak et al. (2009) and Daigne et al. (2011)), and we folded their spectra with the response of the *Fermi* GBM and LAT. The synthetic spectra obtained from these simulations in the keV-MeV domain, where the synchrotron emission is dominant, were used to build a new GRB spectral fitting function called ISSM, which has the same number of parameters as the Band function. We used the ISSM function to fit the prompt emission spectra for a sample of 74 GBM fluent bursts, which improved the fit quality as compared to the phenomenological Band function in a sizeable number of cases. In addition, we combined the ISSM function with a CUTBPL spectral component to fit the GRB 090926A broadband spectrum with some success. This work was motivated by a previous study of this burst that suggested an internal origin of the keV to GeV emission observed during the prompt phase (Y17). In this framework, our interpretation of both spectral components as being from synchrotron and inverse Compton emissions would greatly benefit from a more realistic parameterization of the high-energy component based on the synthetic spectra, especially in the overlapping region at MeV energies.

The analysis of the GBM sample of 74 bursts showed noticeable differences between the ISSM and Band fits. Peak energies and spectral sharpness angles that are obtained from the ISSM fits are slightly larger than those from the Band fits. This result can be attributed to the continuous curvature of the ISSM function. This curvature reflects the time evolution of the electron and photon energy distributions within the analysed time intervals, which lasts longer than the typical dynamical timescales in the physical model. While observed spectra can be well fitted by the ISSM physical function, they appear narrower than the synthetic spectra, essentially because of a theoretical low-energy photon index that differs significantly from the observed photon index α . This problem clearly calls for improvements of the internal shock model and possible solutions have been identified. In particular, more sophisticated prescriptions for the jet physics should be investigated in the future, such as the marginally fast-cooling regime and the decay of the magnetic field behind the shocks. Inferring the parameters of the physical model from the fitted parameters of the ISSM function is not easy as their relation is complex. Actually, the physical parameters that best reproduce GRB prompt emission spectra should be rather explored by fitting the numerical model directly to the data in the future, without using the ISSM proxy function. On the experimental side, complementary multi-wavelength observations will be also performed by GRB-dedicated missions such as SVOM which will observe the complete time evolution of GRBs from possible precursors until the afterglow phase (Wei et al. 2016). SVOM will measure GRB prompt emission spectra down to 4 keV thanks to its ECLAIRs coded-mask telescope, and up to the MeV range with its Gamma-Ray Monitor detector (Bernardini et al. 2017). This will provide more insight into the physical origin of GRB high-energy emission at early times.

Acknowledgements. The *Fermi* LAT Collaboration acknowledges generous ongoing support from a number of agencies and institutes that have supported both the development and the operation of the LAT as well as scientific data analysis. These include the National Aeronautics and Space Administration and the Department of Energy in the United States, the Commissariat à l’Energie Atomique and the Centre National de la Recherche Scientifique / Institut National de Physique Nucléaire et de Physique des Particules in France, the Agenzia Spaziale Italiana and the Istituto Nazionale di Fisica Nucleare in Italy, the Ministry of Education, Culture, Sports, Science and Technology (MEXT), High Energy Accelerator Research Organization (KEK) and Japan Aerospace Exploration Agency (JAXA) in Japan, and the K. A. Wallenberg Foundation, the Swedish Research Council and the Swedish National Space Board in Sweden. Additional support for science analysis during the operations phase is gratefully acknowledged from the Istituto Nazionale di Astrofisica in Italy and the Centre National d’Études Spatiales in France.

Appendix A: Spectral analysis results

Table A.1. Results of the Band and ISSM fits for GRB_B001 in the four time intervals. The true peak energies are $E_{p,true} = 1150, 478, 114$ and 745 keV for the time intervals [0 s, 1 s], [1 s, 3 s], [3 s, 6 s] and [0 s, 6 s] respectively.

Time interval	Model	E_p	$E_p/E_{p,true}$	α	β ($\times 10^{-3} \text{ cm}^{-2} \text{ s}^{-1} \text{ keV}^{-1}$)	Amplitude
[0 s, 1 s]	Band	761 ± 14	0.66	-1.14 ± 0.01	-2.16 ± 0.01	1962 ± 10
	ISSM	1216 ± 25	1.06	-1.07 ± 0.01	-2.45 ± 0.02	36 ± 1
[1 s, 3 s]	Band	295 ± 3	0.62	-1.22 ± 0.01	-2.13 ± 0.01	3100 ± 19
	ISSM	459 ± 6	0.96	-1.09 ± 0.01	-2.35 ± 0.01	145 ± 1
[3 s, 6 s]	Band	99 ± 3	0.87	-1.37 ± 0.02	-2.16 ± 0.01	477 ± 15
	ISSM	119 ± 3	1.04	-0.95 ± 0.08	-2.29 ± 0.02	192 ± 1
[0 s, 6 s]	Band	378 ± 4	0.51	-1.27 ± 0.01	-2.09 ± 0.01	1465 ± 6
	ISSM	659 ± 9	0.88	-1.16 ± 0.01	-2.28 ± 0.01	34 ± 1

Table A.2. Results of the Band and ISSM fits for GRB_B010 in the four time intervals. The true peak energies are $E_{p,true} = 1150, 478, 114$ and 745 keV for the time intervals [0 s, 1 s], [1 s, 3 s], [3 s, 6 s] and [0 s, 6 s] respectively.

Time interval	Model	E_p	$E_p/E_{p,true}$	α	β ($\times 10^{-3} \text{ cm}^{-2} \text{ s}^{-1} \text{ keV}^{-1}$)	Amplitude
[0 s, 1 s]	Band	677 ± 40	0.59	-1.13 ± 0.01	-2.11 ± 0.04	2008 ± 37
	ISSM	1178 ± 82	1.02	-1.06 ± 0.02	-2.41 ± 0.07	35 ± 1
[1 s, 3 s]	Band	298 ± 11	0.62	-1.23 ± 0.01	-2.13 ± 0.02	3077 ± 58
	ISSM	470 ± 18	0.98	-1.08 ± 0.03	-2.33 ± 0.03	145 ± 2
[3 s, 6 s]	Band	104 ± 11	0.91	-1.44 ± 0.05	-2.13 ± 0.03	424 ± 41
	ISSM	127 ± 11	1.11	-1.02 ± 0.27	-2.23 ± 0.05	187 ± 3
[0 s, 6 s]	Band	377 ± 13	0.51	-1.27 ± 0.01	-2.07 ± 0.02	1456 ± 20
	ISSM	685 ± 32	0.92	-1.16 ± 0.02	-2.26 ± 0.03	34 ± 1

Table A.3. Results of the Band and ISSM fits for GRB_B100 in the four time intervals. The true peak energies are $E_{p,true} = 1150, 478, 114$ and 745 keV for the time intervals [0 s, 1 s], [1 s, 3 s], [3 s, 6 s] and [0 s, 6 s] respectively.

Time interval	Model	E_p	$E_p/E_{p,true}$	α	β ($\times 10^{-3} \text{ cm}^{-2} \text{ s}^{-1} \text{ keV}^{-1}$)	Amplitude
[0 s, 1 s]	Band	709 ± 135	0.62	-1.09 ± 0.05	-2.07 ± 0.12	193 ± 11
	ISSM	1333 ± 324	1.16	-1.03 ± 0.08	-2.40 ± 0.24	4 ± 1
[1 s, 3 s]	Band	297 ± 37	0.62	-1.25 ± 0.04	-2.13 ± 0.07	301 ± 18
	ISSM	457 ± 50	0.96	-1.18 ± 0.07	-2.45 ± 0.16	14 ± 1
[3 s, 6 s]	Band	55 ± 17	0.48	-0.90 ± 0.38	-2.00 ± 0.06	136 ± 121
	ISSM	130 ± 34	1.14	unconstrained	-2.18 ± 0.13	19 ± 1
[0 s, 6 s]	Band	445 ± 50	0.60	-1.31 ± 0.03	-2.13 ± 0.07	137 ± 5
	ISSM	678 ± 78	0.91	-1.24 ± 0.04	-2.38 ± 0.12	3.5 ± 0.1

Table A.4. Results of the Band and ISSM spectral fits to GBM data for the prompt emission of 74 GRBs. The amplitudes are given in units of $10^{-4} \text{ cm}^{-2} \text{ s}^{-1} \text{ keV}^{-1}$.

GRB name	Models	E_p	α	α_{10}	β	β_b	Amplitude	$PG_{\text{stat}}/\text{DOF}$
<i>Continued on next page</i>								

Table A.4 – *Continued from previous page*

GRB name	Models	E_p	α	α_{10}	β	β_b	Amplitude	$PG_{\text{stat}}/\text{DOF}$
GRB080817161	Band	410 ± 14	-0.96 ± 0.01	-1.00 ± 0.01	-2.32 ± 0.08	-2.32 ± 0.08	145 ± 2	1031 / 469
	ISSM	509 ± 11	-0.88 ± 0.02	-0.93 ± 0.01	-3.13 ± 0.25	-2.03 ± 0.02	8.9 ± 0.2	1021 / 469
GRB080825593	Band	187 ± 7	-0.64 ± 0.03	-0.75 ± 0.02	-2.35 ± 0.10	-2.35 ± 0.10	641 ± 30	1144 / 469
	ISSM	211 ± 5	-0.56 ± 0.06	-0.66 ± 0.04	-5.19 ± 1.22	-2.11 ± 0.03	10.6 ± 0.2	1149 / 469
GRB081125496	Band	183 ± 8	-0.51 ± 0.05	-0.62 ± 0.04	-3.00 ± 0.92	-3.00 ± 0.92	913 ± 72	534 / 351
	ISSM	187 ± 6	-0.40 ± 0.09	-0.51 ± 0.07	-7.06 ± 2.56	-2.67 ± 0.10	10.2 ± 0.7	532 / 351
GRB081207680	Band	705 ± 40	-0.77 ± 0.02	-0.80 ± 0.02	-2.62 ± 0.28	-2.62 ± 0.28	75 ± 1	1794 / 353
	ISSM	868 ± 39	-0.69 ± 0.04	-0.72 ± 0.03	-3.37 ± 0.28	-2.14 ± 0.04	8.6 ± 0.2	1777 / 353
GRB081224887	Band	404 ± 10	-0.71 ± 0.01	-0.75 ± 0.01	-9.09 ± 1.58	-9.09 ± 1.58	372 ± 6	648 / 474
	ISSM	411 ± 7	-0.67 ± 0.01	-0.71 ± 0.01	-10.00 ± 1.50	-5.47 ± 0.03	23.8 ± 0.3	647 / 474
GRB090328401	Band	754 ± 51	-1.05 ± 0.02	-1.07 ± 0.01	-2.44 ± 0.19	-2.44 ± 0.19	98 ± 2	1241 / 473
	ISSM	897 ± 80	-1.04 ± 0.02	-1.05 ± 0.02	-4.37 ± 1.42	-2.15 ± 0.04	9.6 ± 0.2	1243 / 473
GRB090528516	Band	154 ± 7	-0.84 ± 0.04	-0.95 ± 0.04	-2.04 ± 0.05	-2.04 ± 0.05	197 ± 14	2652 / 472
	ISSM	241 ± 24	-0.57 ± 0.14	-0.76 ± 0.08	-2.55 ± 0.18	-1.82 ± 0.04	3.9 ± 0.2	2650 / 472
GRB090618353	Band	164 ± 3	-1.10 ± 0.01	-1.18 ± 0.01	-2.46 ± 0.04	-2.46 ± 0.04	720 ± 15	1229 / 238
	ISSM	171 ± 2	-0.93 ± 0.03	-1.04 ± 0.02	-3.15 ± 0.11	-2.21 ± 0.01	13.0 ± 0.2	1173 / 238
GRB090718762	Band	170 ± 5	-1.11 ± 0.01	-1.19 ± 0.01	-2.69 ± 0.18	-2.69 ± 0.18	312 ± 8	666 / 469
	ISSM	173 ± 2	-1.02 ± 0.02	-1.10 ± 0.01	-4.22 ± 0.57	-2.41 ± 0.03	5.3 ± 0.3	662 / 469
GRB090719063	Band	240 ± 2	-0.54 ± 0.02	-0.62 ± 0.02	-2.95 ± 0.12	-2.95 ± 0.12	1281 ± 30	460 / 354
	ISSM	250 ± 4	-0.45 ± 0.03	-0.53 ± 0.03	-6.62 ± 0.94	-2.59 ± 0.03	30.9 ± 0.6	455 / 354
GRB090809978	Band	175 ± 10	-0.74 ± 0.03	-0.84 ± 0.02	-1.98 ± 0.04	-1.98 ± 0.04	677 ± 35	815 / 471
	ISSM	344 ± 46	-0.40 ± 0.10	-0.62 ± 0.06	-2.37 ± 0.09	-1.75 ± 0.02	16.7 ± 0.5	810 / 471
GRB090829672	Band	196 ± 9	-1.42 ± 0.01	-1.46 ± 0.01	-2.36 ± 0.10	-2.36 ± 0.10	280 ± 8	510 / 237
	ISSM	208 ± 10	-1.33 ± 0.04	-1.39 ± 0.03	-2.64 ± 0.17	-2.14 ± 0.02	8.0 ± 0.2	498 / 237
GRB091003191	Band	397 ± 16	-0.94 ± 0.02	-0.98 ± 0.02	-2.59 ± 0.19	-2.59 ± 0.19	272 ± 7	551 / 355
	ISSM	429 ± 19	-0.92 ± 0.03	-0.95 ± 0.03	-5.95 ± 2.07	-2.34 ± 0.06	16.1 ± 0.5	552 / 355
GRB091120191	Band	136 ± 5	-1.16 ± 0.03	-1.25 ± 0.02	-2.92 ± 0.28	-2.92 ± 0.28	193 ± 9	965 / 470
	ISSM	134 ± 4	-1.08 ± 0.02	-1.17 ± 0.01	-4.83 ± 1.89	-2.61 ± 0.04	2.1 ± 0.3	964 / 470
GRB091128285	Band	192 ± 1	-0.95 ± 0.01	-1.03 ± 0.01	-2.58 ± 0.16	-2.58 ± 0.16	160 ± 1	1037 / 353
	ISSM	199 ± 2	-0.92 ± 0.02	-0.98 ± 0.01	-6.62 ± 1.66	-2.40 ± 0.03	2.8 ± 0.0	1041 / 353
GRB100322045	Band	333 ± 10	-0.88 ± 0.01	-0.93 ± 0.01	-2.20 ± 0.04	-2.20 ± 0.04	307 ± 6	779 / 469
	ISSM	487 ± 23	-0.69 ± 0.03	-0.78 ± 0.02	-2.60 ± 0.07	-1.91 ± 0.02	15.6 ± 0.2	726 / 469
GRB100324172	Band	461 ± 12	-0.58 ± 0.02	-0.62 ± 0.02	-5.60 ± 1.46	-5.60 ± 1.46	369 ± 6	627 / 469
	ISSM	468 ± 9	-0.54 ± 0.02	-0.58 ± 0.02	-10.00 ± 1.50	-4.21 ± 0.04	30.5 ± 0.5	631 / 469
GRB100414097	Band	637 ± 12	-0.53 ± 0.01	-0.56 ± 0.01	-4.95 ± 1.86	-4.95 ± 1.86	349 ± 4	1070 / 471
	ISSM	651 ± 12	-0.49 ± 0.01	-0.52 ± 0.01	-10.00 ± 5.00	-3.88 ± 0.03	46.1 ± 0.3	1090 / 471
GRB100511035	Band	625 ± 38	-1.28 ± 0.01	-1.29 ± 0.01	-9.37 ± 1.37	-9.37 ± 1.37	94 ± 2	798 / 473
	ISSM	656 ± 51	-1.28 ± 0.01	-1.29 ± 0.01	-10.00 ± 1.50	-5.56 ± 0.02	6.8 ± 0.1	798 / 473
GRB100612726	Band	113 ± 2	-0.57 ± 0.04	-0.75 ± 0.03	-2.55 ± 0.07	-2.55 ± 0.07	1290 ± 79	524 / 472
	ISSM	121 ± 2	-0.25 ± 0.04	-0.51 ± 0.02	-3.80 ± 0.32	-2.23 ± 0.02	6.3 ± 0.6	528 / 472
GRB100707032	Band	266 ± 14	-0.69 ± 0.03	-0.76 ± 0.02	-2.08 ± 0.05	-2.08 ± 0.05	236 ± 10	450 / 236
	ISSM	504 ± 61	-0.36 ± 0.08	-0.52 ± 0.06	-2.39 ± 0.10	-1.79 ± 0.02	9.7 ± 0.2	440 / 236
GRB100719989	Band	321 ± 12	-0.69 ± 0.03	-0.74 ± 0.02	-2.41 ± 0.08	-2.41 ± 0.08	462 ± 15	733 / 354
	ISSM	384 ± 13	-0.56 ± 0.04	-0.63 ± 0.03	-3.55 ± 0.34	-2.07 ± 0.03	22.4 ± 0.4	726 / 354

Continued on next page

Table A.4 – *Continued from previous page*

GRB name	Models	E_p	α	α_{10}	β	β_b	Amplitude	$PG_{\text{stat}}/\text{DOF}$
GRB100826957	Band	461 ± 25	-1.05 ± 0.01	-1.08 ± 0.01	-2.05 ± 0.02	-2.05 ± 0.02	310 ± 5	717 / 237
	ISSM	1005 ± 77	-0.95 ± 0.02	-1.00 ± 0.02	-2.30 ± 0.04	-1.80 ± 0.02	21.1 ± 0.2	696 / 237
GRB100829876	Band	136 ± 5	-0.60 ± 0.08	-0.75 ± 0.06	-2.04 ± 0.04	-2.04 ± 0.04	946 ± 104	276 / 237
	ISSM	232 ± 29	-0.15 ± 0.09	-0.48 ± 0.03	-2.49 ± 0.16	-1.77 ± 0.06	13.8 ± 0.8	275 / 237
GRB100910818	Band	159 ± 10	-0.94 ± 0.01	-1.03 ± 0.00	-2.46 ± 0.11	-2.46 ± 0.11	376 ± 8	587 / 469
	ISSM	168 ± 2	-0.84 ± 0.03	-0.94 ± 0.02	-4.42 ± 0.78	-2.25 ± 0.03	5.1 ± 0.4	586 / 469
GRB100918863	Band	562 ± 3	-0.80 ± 0.01	-0.84 ± 0.00	-2.74 ± 0.12	-2.74 ± 0.12	205 ± 1	709 / 352
	ISSM	612 ± 10	-0.76 ± 0.01	-0.79 ± 0.01	-5.05 ± 0.14	-2.37 ± 0.02	18.9 ± 0.2	714 / 352
GRB101014175	Band	210 ± 4	-1.17 ± 0.01	-1.22 ± 0.01	-2.79 ± 0.11	-2.79 ± 0.11	625 ± 12	356 / 237
	ISSM	218 ± 5	-1.16 ± 0.01	-1.20 ± 0.01	-9.04 ± 3.19	-2.61 ± 0.02	14.6 ± 0.4	365 / 237
GRB101023951	Band	185 ± 7	-1.22 ± 0.03	-1.28 ± 0.02	-2.58 ± 0.14	-2.58 ± 0.14	220 ± 10	1653 / 353
	ISSM	187 ± 6	-1.12 ± 0.03	-1.19 ± 0.02	-3.61 ± 0.48	-2.33 ± 0.04	4.7 ± 0.2	1649 / 353
GRB101126198	Band	135 ± 1	-1.29 ± 0.01	-1.37 ± 0.00	-2.65 ± 0.17	-2.65 ± 0.17	211 ± 1	890 / 470
	ISSM	140 ± 1	-1.28 ± 0.01	-1.34 ± 0.01	-8.81 ± 0.29	-2.51 ± 0.01	2.5 ± 0.1	893 / 470
GRB101231067	Band	214 ± 2	-0.75 ± 0.02	-0.83 ± 0.01	-9.99 ± 4.99	-9.99 ± 4.99	251 ± 3	531 / 353
	ISSM	216 ± 4	-0.70 ± 0.04	-0.78 ± 0.03	-8.07 ± 2.97	-5.19 ± 0.07	4.6 ± 0.2	531 / 353
GRB110301214	Band	110 ± 1	-0.83 ± 0.02	-0.99 ± 0.02	-2.73 ± 0.05	-2.73 ± 0.05	4242 ± 124	713 / 470
	ISSM	110 ± 2	-0.59 ± 0.04	-0.80 ± 0.03	-4.03 ± 0.18	-2.42 ± 0.01	22.0 ± 0.9	690 / 470
GRB110622158	Band	105 ± 1	-0.64 ± 0.03	-0.83 ± 0.02	-2.44 ± 0.04	-2.44 ± 0.04	541 ± 25	1973 / 471
	ISSM	114 ± 2	-0.17 ± 0.06	-0.52 ± 0.03	-3.28 ± 0.14	-2.15 ± 0.01	2.9 ± 0.1	1997 / 471
GRB110625881	Band	179 ± 4	-0.77 ± 0.02	-0.87 ± 0.01	-2.33 ± 0.04	-2.33 ± 0.04	929 ± 26	1285 / 470
	ISSM	210 ± 3	-0.53 ± 0.05	-0.68 ± 0.03	-3.16 ± 0.14	-2.05 ± 0.01	17.4 ± 0.3	1250 / 470
GRB110717319	Band	376 ± 5	-1.01 ± 0.01	-1.05 ± 0.01	-9.37 ± 1.57	-9.37 ± 1.57	98 ± 1	813 / 470
	ISSM	370 ± 7	-0.98 ± 0.01	-1.01 ± 0.01	-10.00 ± 1.50	-5.69 ± 0.02	5.1 ± 0.1	813 / 470
GRB110729142	Band	307 ± 11	-1.02 ± 0.02	-1.07 ± 0.01	-2.21 ± 0.15	-2.21 ± 0.15	35 ± 1	838 / 473
	ISSM	390 ± 26	-0.91 ± 0.07	-0.97 ± 0.06	-2.89 ± 0.31	-1.98 ± 0.03	1.6 ± 0.0	835 / 473
GRB110731465	Band	307 ± 15	-0.87 ± 0.02	-0.92 ± 0.02	-2.88 ± 0.65	-2.88 ± 0.65	565 ± 14	423 / 354
	ISSM	322 ± 9	-0.86 ± 0.02	-0.90 ± 0.02	-10.00 ± 1.50	-2.64 ± 0.04	23.3 ± 0.6	427 / 354
GRB110825102	Band	262 ± 2	-1.07 ± 0.01	-1.12 ± 0.01	-2.72 ± 0.31	-2.72 ± 0.31	177 ± 1	697 / 473
	ISSM	267 ± 1	-1.05 ± 0.01	-1.09 ± 0.01	-10.00 ± 1.50	-2.58 ± 0.02	5.6 ± 0.0	698 / 473
GRB110921912	Band	513 ± 20	-0.88 ± 0.01	-0.91 ± 0.01	-2.36 ± 0.09	-2.36 ± 0.09	283 ± 5	506 / 356
	ISSM	678 ± 43	-0.78 ± 0.04	-0.82 ± 0.03	-2.89 ± 0.19	-2.00 ± 0.03	22.4 ± 0.4	489 / 356
GRB111003465	Band	205 ± 7	-0.95 ± 0.02	-1.02 ± 0.02	-2.43 ± 0.10	-2.43 ± 0.10	394 ± 16	627 / 473
	ISSM	228 ± 9	-0.86 ± 0.06	-0.94 ± 0.04	-3.76 ± 0.57	-2.16 ± 0.04	9.3 ± 0.4	625 / 473
GRB111216389	Band	165 ± 5	-0.91 ± 0.03	-1.00 ± 0.03	-2.30 ± 0.06	-2.30 ± 0.06	199 ± 9	734 / 352
	ISSM	197 ± 7	-0.79 ± 0.07	-0.90 ± 0.05	-3.30 ± 0.30	-2.04 ± 0.02	3.5 ± 0.2	730 / 352
GRB111220486	Band	300 ± 10	-1.05 ± 0.01	-1.09 ± 0.01	-2.30 ± 0.07	-2.30 ± 0.07	308 ± 6	474 / 353
	ISSM	371 ± 15	-0.96 ± 0.01	-1.02 ± 0.00	-3.01 ± 0.15	-2.03 ± 0.02	13.2 ± 0.2	467 / 353
GRB120119170	Band	208 ± 1	-1.03 ± 0.01	-1.09 ± 0.01	-2.54 ± 0.10	-2.54 ± 0.10	207 ± 1	774 / 469
	ISSM	226 ± 3	-0.97 ± 0.01	-1.04 ± 0.01	-4.37 ± 0.30	-2.27 ± 0.02	5.0 ± 0.0	773 / 469
GRB120129580	Band	299 ± 7	-0.68 ± 0.02	-0.74 ± 0.02	-2.56 ± 0.07	-2.56 ± 0.07	3845 ± 100	392 / 236
	ISSM	337 ± 8	-0.47 ± 0.03	-0.56 ± 0.03	-3.28 ± 0.18	-2.16 ± 0.02	157.3 ± 2.4	346 / 236
GRB120204054	Band	163 ± 2	-1.08 ± 0.01	-1.16 ± 0.01	-2.58 ± 0.05	-2.58 ± 0.05	612 ± 11	1763 / 470
	ISSM	171 ± 3	-1.01 ± 0.02	-1.09 ± 0.02	-4.31 ± 0.30	-2.33 ± 0.01	9.7 ± 0.2	1760 / 470

Continued on next page

Table A.4 – *Continued from previous page*

GRB name	Models	E_p	α	α_{10}	β	β_b	Amplitude	$PG_{\text{stat}}/\text{DOF}$
GRB120226871	Band	301 ± 11	-0.89 ± 0.02	-0.94 ± 0.02	-2.26 ± 0.08	-2.26 ± 0.08	231 ± 8	1338 / 470
	ISSM	397 ± 21	-0.76 ± 0.04	-0.83 ± 0.03	-2.89 ± 0.22	-1.96 ± 0.02	10.3 ± 0.2	1318 / 470
GRB120328268	Band	194 ± 4	-0.78 ± 0.02	-0.87 ± 0.01	-2.00 ± 0.02	-2.00 ± 0.02	799 ± 21	1414 / 471
	ISSM	385 ± 23	-0.47 ± 0.05	-0.66 ± 0.02	-2.35 ± 0.05	-1.76 ± 0.03	22.7 ± 0.3	1357 / 471
GRB120426090	Band	135 ± 3	-0.59 ± 0.03	-0.74 ± 0.02	-2.94 ± 0.12	-2.94 ± 0.12	4721 ± 208	524 / 352
	ISSM	132 ± 3	-0.28 ± 0.07	-0.49 ± 0.05	-4.49 ± 0.42	-2.55 ± 0.03	27.1 ± 1.6	501 / 352
GRB120624933	Band	583 ± 83	-0.97 ± 0.05	-0.99 ± 0.05	-2.05 ± 0.16	-2.05 ± 0.16	18 ± 1	2055 / 469
	ISSM	1107 ± 457	-0.96 ± 0.07	-0.98 ± 0.07	-2.62 ± 0.51	-1.76 ± 0.10	1.6 ± 0.1	2058 / 469
GRB120707800	Band	181 ± 13	-1.08 ± 0.03	-1.15 ± 0.03	-2.37 ± 0.05	-2.37 ± 0.05	708 ± 29	1173 / 352
	ISSM	189 ± 6	-0.76 ± 0.10	-0.91 ± 0.19	-2.83 ± 0.13	-2.14 ± 0.06	15.2 ± 0.3	1167 / 352
GRB120711115	Band	1277 ± 31	-0.95 ± 0.01	-0.96 ± 0.01	-3.11 ± 0.13	-3.11 ± 0.13	385 ± 2	577 / 353
	ISSM	1360 ± 27	-0.95 ± 0.01	-0.96 ± 0.01	-8.68 ± 1.64	-2.75 ± 0.02	54.7 ± 0.2	594 / 353
GRB130306991	Band	307 ± 15	-0.75 ± 0.03	-0.81 ± 0.03	-2.62 ± 0.11	-2.62 ± 0.11	301 ± 6	2204 / 470
	ISSM	323 ± 5	-0.50 ± 0.11	-0.59 ± 0.11	-3.70 ± 0.24	-2.28 ± 0.11	12.6 ± 0.2	2200 / 470
GRB130327350	Band	375 ± 8	-0.61 ± 0.02	-0.66 ± 0.01	-9.37 ± 2.22	-9.37 ± 2.22	287 ± 5	1057 / 470
	ISSM	379 ± 8	-0.57 ± 0.02	-0.61 ± 0.02	-10.00 ± 1.50	-5.54 ± 0.03	16.7 ± 0.3	1063 / 470
GRB130502327	Band	293 ± 5	-0.50 ± 0.01	-0.57 ± 0.01	-2.36 ± 0.04	-2.36 ± 0.04	972 ± 16	1361 / 473
	ISSM	354 ± 5	-0.35 ± 0.02	-0.44 ± 0.02	-3.72 ± 0.16	-2.02 ± 0.01	41.6 ± 0.4	1338 / 473
GRB130504978	Band	654 ± 29	-1.20 ± 0.01	-1.21 ± 0.01	-2.27 ± 0.07	-2.27 ± 0.07	232 ± 2	2120 / 470
	ISSM	867 ± 41	-1.18 ± 0.01	-1.19 ± 0.01	-3.05 ± 0.17	-2.00 ± 0.01	18.1 ± 0.2	2125 / 470
GRB130518580	Band	387 ± 10	-0.87 ± 0.01	-0.91 ± 0.01	-2.22 ± 0.05	-2.22 ± 0.05	330 ± 6	768 / 354
	ISSM	539 ± 20	-0.78 ± 0.02	-0.83 ± 0.02	-2.93 ± 0.14	-1.92 ± 0.02	20.3 ± 0.2	769 / 354
GRB130606497	Band	515 ± 21	-1.13 ± 0.01	-1.15 ± 0.01	-2.10 ± 0.02	-2.10 ± 0.02	544 ± 6	892 / 236
	ISSM	926 ± 43	-1.03 ± 0.01	-1.07 ± 0.01	-2.35 ± 0.04	-1.86 ± 0.01	37.5 ± 0.3	919 / 236
GRB130609902	Band	531 ± 13	-0.98 ± 0.02	-1.01 ± 0.02	-9.37 ± 1.77	-9.37 ± 1.77	47 ± 1	822 / 354
	ISSM	539 ± 31	-0.96 ± 0.02	-0.98 ± 0.01	-9.37 ± 3.80	-5.45 ± 0.03	3.7 ± 0.1	822 / 354
GRB130720582	Band	65 ± 3	-0.95 ± 0.03	-1.18 ± 0.03	-2.39 ± 0.02	-2.39 ± 0.02	451 ± 24	2608 / 469
	ISSM	66 ± 1	-0.19 ± 0.05	-0.83 ± 0.06	-2.86 ± 0.03	-2.16 ± 0.01	1.7 ± 0.0	2570 / 469
GRB131028076	Band	848 ± 15	-0.64 ± 0.01	-0.66 ± 0.01	-2.55 ± 0.03	-2.55 ± 0.03	791 ± 6	1132 / 353
	ISSM	952 ± 9	-0.61 ± 0.00	-0.63 ± 0.00	-6.16 ± 0.22	-2.24 ± 0.01	125.0 ± 0.5	2119 / 353
GRB131118958	Band	332 ± 14	-0.69 ± 0.02	-0.75 ± 0.02	-9.37 ± 1.67	-9.37 ± 1.67	195 ± 4	1105 / 237
	ISSM	313 ± 9	-0.39 ± 0.13	-0.47 ± 0.26	-4.43 ± 0.87	-3.72 ± 0.26	8.6 ± 0.2	1092 / 237
GRB131231198	Band	218 ± 6	-1.20 ± 0.01	-1.25 ± 0.01	-2.41 ± 0.04	-2.41 ± 0.04	1119 ± 18	1350 / 355
	ISSM	232 ± 4	-1.08 ± 0.02	-1.15 ± 0.05	-3.10 ± 0.13	-2.17 ± 0.05	31.5 ± 0.3	1315 / 355
GRB140306146	Band	1529 ± 73	-1.01 ± 0.01	-1.02 ± 0.01	-5.09 ± 1.80	-5.09 ± 1.80	126 ± 1	1492 / 355
	ISSM	1535 ± 62	-1.00 ± 0.01	-1.01 ± 0.01	-10.00 ± 1.50	-4.05 ± 0.02	17.7 ± 0.2	1495 / 355
GRB140416060	Band	97 ± 3	-1.15 ± 0.01	-1.27 ± 0.01	-2.37 ± 0.03	-2.37 ± 0.03	1056 ± 75	2323 / 237
	ISSM	101 ± 3	-0.86 ± 0.06	-1.08 ± 0.12	-2.93 ± 0.11	-2.16 ± 0.06	9.8 ± 0.2	2315 / 237
GRB140508128	Band	264 ± 13	-1.01 ± 0.02	-1.07 ± 0.02	-2.11 ± 0.04	-2.11 ± 0.04	312 ± 11	1153 / 235
	ISSM	434 ± 44	-0.83 ± 0.06	-0.93 ± 0.04	-2.41 ± 0.10	-1.87 ± 0.02	12.4 ± 0.2	1164 / 235
GRB140523129	Band	269 ± 7	-0.90 ± 0.01	-0.96 ± 0.01	-2.69 ± 0.13	-2.69 ± 0.13	632 ± 9	765 / 471
	ISSM	285 ± 4	-0.83 ± 0.01	-0.89 ± 0.01	-4.71 ± 0.37	-2.38 ± 0.01	21.4 ± 0.3	760 / 471
GRB140810782	Band	309 ± 6	-0.88 ± 0.01	-0.93 ± 0.01	-2.41 ± 0.06	-2.41 ± 0.06	286 ± 5	896 / 353
	ISSM	368 ± 14	-0.75 ± 0.03	-0.81 ± 0.03	-3.17 ± 0.20	-2.08 ± 0.03	12.6 ± 0.2	871 / 353

Continued on next page

Table A.4 – Continued from previous page

GRB name	Models	E_p	α	α_{10}	β	β_b	Amplitude	$PG_{\text{stat}}/\text{DOF}$
GRB150118409	Band	763 ± 17	-0.84 ± 0.01	-0.86 ± 0.01	-3.51 ± 0.25	-3.51 ± 0.25	332 ± 3	2545 / 469
	ISSM	795 ± 18	-0.83 ± 0.01	-0.84 ± 0.01	-10.00 ± 1.50	-3.07 ± 0.02	39.9 ± 0.3	2558 / 469
GRB150330828	Band	265 ± 5	-1.01 ± 0.01	-1.06 ± 0.01	-2.25 ± 0.04	-2.25 ± 0.04	202 ± 3	1708 / 469
	ISSM	346 ± 11	-0.90 ± 0.02	-0.97 ± 0.02	-2.86 ± 0.13	-1.98 ± 0.01	7.7 ± 0.1	1683 / 469
GRB150403913	Band	402 ± 16	-0.82 ± 0.02	-0.86 ± 0.02	-2.09 ± 0.04	-2.09 ± 0.04	437 ± 10	624 / 355
	ISSM	721 ± 45	-0.67 ± 0.03	-0.74 ± 0.02	-2.49 ± 0.07	-1.80 ± 0.02	29.0 ± 0.4	578 / 355
GRB150627183	Band	243 ± 5	-0.92 ± 0.01	-0.98 ± 0.01	-2.19 ± 0.02	-2.19 ± 0.02	664 ± 11	1109 / 355
	ISSM	334 ± 8	-0.76 ± 0.02	-0.86 ± 0.01	-2.73 ± 0.07	-1.93 ± 0.01	23.0 ± 0.2	1057 / 355
GRB150902733	Band	368 ± 7	-0.49 ± 0.01	-0.55 ± 0.01	-2.35 ± 0.04	-2.35 ± 0.04	1085 ± 17	761 / 470
	ISSM	472 ± 7	-0.30 ± 0.03	-0.38 ± 0.02	-3.24 ± 0.10	-1.97 ± 0.01	68.3 ± 0.6	656 / 470
GRB160802259	Band	295 ± 5	-0.54 ± 0.02	-0.62 ± 0.02	-2.47 ± 0.07	-2.47 ± 0.07	863 ± 20	314 / 237
	ISSM	346 ± 9	-0.40 ± 0.01	-0.49 ± 0.01	-3.73 ± 0.13	-2.10 ± 0.02	36.2 ± 0.7	298 / 237
GRB160905471	Band	1063 ± 52	-0.89 ± 0.01	-0.90 ± 0.01	-3.01 ± 0.27	-3.01 ± 0.27	237 ± 2	730 / 356
	ISSM	1161 ± 20	-0.89 ± 0.01	-0.90 ± 0.01	-10.00 ± 0.00	-2.66 ± 0.02	33.5 ± 0.2	736 / 356
GRB160910722	Band	335 ± 7	-0.76 ± 0.01	-0.82 ± 0.01	-2.23 ± 0.03	-2.23 ± 0.03	632 ± 11	786 / 469
	ISSM	460 ± 11	-0.60 ± 0.02	-0.67 ± 0.04	-2.85 ± 0.08	-1.92 ± 0.02	33.1 ± 0.3	746 / 469

References

- Abbott, B. P., Abbott, R., Abbott, T. D., et al. 2017, *ApJ*, 848, L13
- Abdo, A. A., Ackermann, M., Ajello, M., Asano, K., & Atwood, W. B., e. a. 2009, *APJL*, 706, L138
- Ackermann, M., Ajello, M., Asano, K., Axelsson, M., & Baldini, L., e. a. 2011, *APJ*, 729, 114
- Ackermann, M., Ajello, M., Asano, K., et al. 2013, *APJS*, 209, 11
- Ajello, M., Arimoto, M., Axelsson, M., et al. 2019, *ApJ*, 878, 52
- Atwood, W. B., Abdo, A. A., Ackermann, M., et al. 2009, *ApJ*, 697, 1071
- Atwood, W. B., Baldini, L., Bregeon, J., et al. 2013, *ApJ*, 774, 76
- Axelsson, M., Baldini, L., Barbiellini, G., Baring, M. G., & Bellazzini, R., e. a. 2012, *APJL*, 757, L31
- Axelsson, M. & Borgonovo, L. 2015, *MNRAS*, 447, 3150
- Band, D., Matteson, J., Ford, L., Schaefer, B., & Palmer, D., e. a. 1993, *APJ*, 413, 281
- Beloborodov, A. M. & Mészáros, P. 2017, *Space Sci. Rev.*, 207, 87
- Beniamini, P. & Granot, J. 2016, *MNRAS*, 459, 3635
- Beniamini, P. & Piran, T. 2013, *ApJ*, 769, 69
- Bernardini, M. G., Xie, F., Sizun, P., et al. 2017, *Experimental Astronomy*, 44, 113
- Bloom, J. S., Kulkarni, S. R., Price, P. A., et al. 2002, *ApJ*, 572, L45
- Bošnjak, Ž. & Daigne, F. 2014, *A&A*, 568, A45
- Bošnjak, Ž., Daigne, F., & Dubus, G. 2009, *A&A*, 498, 677
- Burgess, J. M. 2019, *A&A*, 629, A69
- Burgess, J. M., Ryde, F., & Yu, H.-F. 2015, *MNRAS*, 451, 1511
- Crider, A., Liang, E. P., Smith, I. A., et al. 1997, *ApJ*, 479, L39
- Daigne, F., Bošnjak, Ž., & Dubus, G. 2011, *A&A*, 526, A110
- Daigne, F. & Mochkovitch, R. 1998, *MNRAS*, 296, 275
- D’Avanzo, P. 2015, *Journal of High Energy Astrophysics*, 7, 73
- Derishev, E. V. 2007, *Ap&SS*, 309, 157
- Gehrels, N., Sarazin, C. L., O’Brien, P. T., et al. 2005, *Nature*, 437, 851
- Ghisellini, G., Celotti, A., & Lazzati, D. 2000, *MNRAS*, 313, L1
- Giannios, D. 2008, *A&A*, 480, 305
- Gruber, D., Goldstein, A., Weller von Ahlefeld, V., Narayana Bhat, P., & Bissaldi, E., e. a. 2014, *APJS*, 211, 12
- Guiriec, S., Connaughton, V., Briggs, M. S., Burgess, M., & Ryde, F., e. a. 2011, *APJL*, 727, L33
- Guiriec, S., Kouveliotou, C., Daigne, F., Zhang, B., & Hascoët, R., e. a. 2015, *APJ*, 807, 148
- Hjorth, J., Sollerman, J., Gorosabel, J., et al. 2005, *ApJ*, 630, L117
- Hjorth, J., Sollerman, J., Möller, P., et al. 2003, *Nature*, 423, 847
- Kawabata, K. S., Deng, J., Wang, L., et al. 2003, *ApJ*, 593, L19
- Kobayashi, S., Piran, T., & Sari, R. 1997, *ApJ*, 490, 92
- Massaro, F., Grindlay, J. E., & Paggi, A. 2010, *APJL*, 714, L299
- McKinney, J. C. & Uzdensky, D. A. 2012, *MNRAS*, 419, 573
- Nakar, E. 2007, *Phys. Rep.*, 442, 166
- Narayana Bhat, P., Meegan, C. A., von Kienlin, A., et al. 2016, *ApJS*, 223, 28
- Neyman, J. & Pearson, E. S. 1928, *On the Use and Interpretation of Certain Test Criteria for Purposes of Statistical Inference, Part I* (London: Cambridge University Press)
- Pe’er, A. & Zhang, B. 2006, *ApJ*, 653, 454
- Preece, R. D., Briggs, M. S., Malozzi, R. S., Pendleton, G. N., & Paciesas, W. S., e. a. 1998, *APJL*, 506, L23
- Rees, M. J. & Meszaros, P. 1994, *ApJ*, 430, L93
- Sironi, L., Petropoulou, M., & Giannios, D. 2015, *MNRAS*, 450, 183

- Stanek, K. Z., Matheson, T., Garnavich, P. M., et al. 2003, *ApJ*, 591, L17
- Tierney, D., McBreen, S., Preece, R. D., Fitzpatrick, G., & Foley, S., e. a. 2013, *AAP*, 550, A102
- Wei, J., Cordier, B., Antier, S., et al. 2016, *The Deep and Transient Universe in the SVOM Era: New Challenges and Opportunities - Scientific prospects of the SVOM mission*, report on the Scientific prospects of the SVOM mission. Proceedings of the Workshop held from 11th to 15th April 2016 at Les Houches School of Physics, France
- Wilks, S. S. 1938, *Ann. Math. Statist.*, 9, 60
- Woosley, S. E. & Bloom, J. S. 2006, *ARA&A*, 44, 507
- Yassine, M., Piron, F., Mochkovitch, R., & Daigne, F. 2017, *A&A*, 606, A93
- Yu, H.-F., van Eerten, H. J., Greiner, J., Sari, R., & Narayana Bhat, P., e. a. 2015, *AAP*, 583, A129
- Zhang, B.-B., Uhm, Z. L., Connaughton, V., Briggs, M. S., & Zhang, B. 2016, *ApJ*, 816, 72